Final Report of Contract NAG3-2221 Date: November 2001

Numerical Study of Buoyancy and Different Diffusion Effects on the Structure and Dynamics of Triple Flames

J.-Y. Chen* and Tarek Echekki[+]

*Department of Mechanical Engineering
University of California at Berkeley
Berkeley, CA 94720-1740, USA

[+]Combustion Research Facility, MS 9051
Sandia National Laboratories
Livermore, CA 94551-0969, USA

Abstract

Numerical simulations of 2-D triple flames under gravity force have been implemented to identify the effects of gravity on triple flame structure and propagation properties and to understand the mechanisms of instabilities resulting from both heat release and buoyancy effects. A wide range of gravity conditions, heat release, and mixing widths for a scalar mixing layer are computed for downward-propagating (in the same direction with the gravity vector) and upward-propagating (in the opposite direction of the gravity vector) triple flames.

Results of numerical simulations show that gravity strongly affects the triple flame speed through its contribution to the overall flow field. A simple analytical model for the triple flame speed, which accounts for both buoyancy and heat release, is developed. Comparisons of the proposed model with the numerical results for a wide range of gravity, heat release and mixing width conditions, yield very good agreement. The analysis shows that under neutral diffusion, downward propagation reduces the triple flame speed, while upward propagation enhances it. For the former condition, a critical Froude number may be evaluated, which corresponds to a vanishing triple flame speed.

Downward-propagating triple flames at relatively strong gravity effects have exhibited instabilities. These instabilities are generated without any artificial forcing of the flow. Instead disturbances are initiated by minute round-off errors in the numerical simulations, and subsequently amplified by instabilities. A linear stability analysis on mean profiles of stable triple flame configurations have been performed to identify the most amplified frequency in spatially developed flows. The eigenfunction equations obtained from the linearized disturbance equations are solved using the shooting method. The linear stability analysis yields reasonably good agreements with the observed frequencies of the unstable triple flames. The frequencies and amplitudes of disturbances increase with the magnitude of the gravity vector. Moreover, disturbances appear to be most amplified just downstream of the premixed branches. The effects of mixing width and differential diffusion are investigated and their roles on the flame stability are studied.

Introduction

Since the work of Phillips [1] more than three decades ago, there has been a growing interest in the study of triple flames [2-17]. The interest is largely motivated by the potential role these structures play in the burning of partially premixed mixtures, especially for the stabilization and ignition in diffusion flames (e.g., [1], [9], [18]). Heat release is known to play an important role in the enhancement of the triple flame propagation speed as demonstrated by the numerical studies of Ruetsch et al. [11]. Analyses and computations in [15] shows that under strain and non-unity Lewis number conditions a significant departure of the triple flame speed from the laminar planar value may occur even in the absence of heat release. More recently, Echekki and Chen [16] and Im and Chen [19] explored the coupling of heat release with preferential diffusion effects and chemistry. Their studies show that to the first order, the enhancement of the triple flame speed is primarily attributed to heat release. The contribution of preferential diffusion to the triple flame speed especially near the leading edge (the triple point) of the triple flame is within 10% or less. The above-mentioned studies also show that the triple flame propagation speed can be approximated by the square root of the density ratio across the triple flame as proposed by Ruetsch et al [11]. This simple correlation is valid for the range of moderate scalar mixing layer thickness. The physical mechanism that contributes to the enhancement of the triple flame speed with heat release is directly associated with the streamline divergence ahead of the premixed branches followed by their subsequent convergence further downstream.

Because of the role played by the fluid mechanics in the enhancement of the triple flame speed, the coupling between heat release and gravity is believed to be important. This coupling is also believed to play a key role in the onset of instabilities in triple flames. Recently, measurements and computations by Aggarwal et al [22] showed that burner-stabilized triple flames in two fuel-oxidizer stream configurations are subject to buoyancy-induced instabilities at normal gravity. They proposed that these instabilities are of the Kelvin-Helmholtz type. They also observed that these instabilities generate large vortex structures that are initiated in the nonpremixed branch in one configuration and in the premixed branch in the other. The corresponding flickering frequencies, which are shown to be of the same order as the ones observed in candle flames and jet diffusion flames, are affected by the amount of heat release as seen in the two configurations.

Heat release and buoyancy have long been recognized to play key roles in the onset and damping of instabilities in premixed and diffusion flames. For example, these instabilities are associated with the flickering of the candle flame [35, 36] or the instabilities in premixed bluff body stabilized flames [37]. Various approaches have been used to identify the origins of these instabilities. In this investigation, we attempt to elucidate the nature of the coupling between heat release and buoyancy by computational studies of the structure, propagation and stability characteristics of triple flames in a scalar mixing layer. First, we will consider a diffusion neutral mixture (the Lewis numbers of both fuel and oxidizer are equal to unity) with a simple finite-rate kinetic model. Consideration of differential diffusion effects in terms of Lewis number will be given as well. Moreover, triple flame configurations with the gravity vector aligned with the axis of triple flame propagation are extensively examined. A parametric study is carried out with the magnitude and sign of the gravity vector varied over a relatively wide range of conditions. For stability analysis, we formulate a triple flame inviscid linear stability analysis. We will attempt to

identify the mechanisms of buoyancy-induced instabilities and evaluate the most amplified frequencies.

The report is divided two major sections. The first is concerned with the study structure and propagation in steady state triple. The second is focused on transient triple flames and their stability analysis. In the following sections, the governing equations and numerical implementation of the solution of the triple flames are presented. Then, discussions of the computed effects of buoyancy on triple flame structure and propagation are given. Results of a series of parametric runs are presented in the following section to explore the relationship between the triple flame propagation speed and the buoyancy. A simple theory of the dependence of the triple flame speed on the buoyancy and heat release is proposed. The theoretical prediction is compared to the computed triple flame speeds over a wide range of parameters. Next the formulation and computation of linear stability of triple flames are discussed. Finally, a summary of the findings is presented.

Numerical Configuration of the Triple Flame

Simulations of planar triple flames in a scalar-mixing layer are implemented using an unsteady two-dimensional numerical scheme with high accuracy comparable those used for direct numerical simulations for turbulent flows. The governing equations are summarized below.

Continuity: Mass conservation is expressed as follows

$$\frac{\partial \rho}{\partial t} + \frac{\partial \rho u_j}{\partial x_j} = 0 \tag{1}$$

and u_1 and u_2 correspond to the streamwise velocity and transverse velocity respectively. Here, the streamwise coordinate will be denoted by x and the transverse coordinate by y.

Momentum: The momentum equation for the 2-D compressible flow is expressed as follows

$$\frac{\partial \rho u_i}{\partial t} + \frac{\partial \rho u_i u_j}{\partial x_j} = -\frac{\partial p}{\partial x_i} + \frac{\partial \tau_{ij}}{\partial x_j} - \rho \delta_{1i} g , \tag{2}$$

where g is the gravity acceleration with a positive value for gravity vector pointed in the same direction as flame propagation. We will denote these flames as downward-propagating triple flames and those with a negative acceleration of gravity as upward-propagating triple flames. The stress tensor, τ_{ij}, is given by:

$$\tau_{ij} = \mu \left[\left(\frac{\partial u_i}{\partial u_j} + \frac{\partial u_j}{\partial u_i} \right) - \frac{2}{3} \delta_{ij} \frac{\partial u_k}{\partial x_k} \right], \tag{3}$$

where μ is the viscosity with temperature dependence as

$$\mu = \mu_0 \left(\frac{T}{T_0} \right)^a \qquad (4)$$

with $a = 0.76$. The reference state, denoted by the subscript 0, corresponds to inlet conditions where the temperature is assumed to be uniform (in the transverse direction).

Energy: Assuming the ideal gas law, $P = \rho R T$, the equation for total energy, e_t, defined as

$$\rho e_t = \frac{1}{2} \rho u_j^2 + \frac{P}{\gamma - 1} \qquad (5)$$

is

$$\frac{\partial \rho e_t}{\partial t} + \frac{\partial (\rho e_t + P) u_j}{\partial x_j} = -\frac{\partial q_j}{\partial x_j} + \frac{\partial u_j \tau_{ij}}{\partial x_j} - Q_F \dot{\omega}_F - \rho \delta_{1j} u_j g , \qquad (6)$$

where γ is the ratio of species heats, c_p/c_v, assumed to have a constant value of 1.4. Q_F is the heat of reaction per unit mass of fuel burned. $\dot{\omega}_F$ is the chemical reaction rate of fuel and q_j is the heat flux in the j-direction given by

$$q_j = -\lambda \frac{\partial T}{\partial x_j} , \qquad (7)$$

where λ is the thermal conductivity.

Species: The combustion process is described by the equations for the fuel and oxidizer mass fractions, Y_F and Y_O, as

$$\frac{\partial \rho Y_k}{\partial t} + \frac{\partial \rho u_j Y_k}{\partial x_j} = -\frac{\partial Y_k V_{jk}}{\partial x_i} + \dot{\omega}_k \qquad (8)$$

Here, V_{jk} is the diffusive flux of species k in the j-direction given by

$$V_{jk} = -\frac{\rho D_k}{Y_k} \frac{\partial Y_k}{\partial x_j} , \qquad (9)$$

where D_k is the mass diffusivity of the species k. The thermal conductivity and mass diffusivities are temperature dependent and their values are determined by assuming constant values of Lewis and Prandtl numbers as

$$Le_F = \frac{\lambda}{\rho C_p D_F} , \quad Le_O = \frac{\lambda}{\rho C_p D_O} , \quad Pr = \frac{\mu C_p}{\lambda} . \qquad (10)$$

In this investigation, we set $Pr=0.75$. The combustion process is modeled by a one-step chemical reaction as

$$F + O \rightarrow P, \tag{11}$$

where the stoichiometric coefficients are unitary for simplicity. The reaction rate has the following Arrhenius form

$$\dot{w} = A\rho Y_F \rho Y_O \exp\left(-\frac{T_a}{T}\right). \tag{12}$$

Here, T_a is the activation temperature and A is the pre-exponential factor. With the non dimensional temperature, θ, the heat release parameter, ϑ, the Zeldovich number, κ, and the reduced pre-exponential factor, Λ, the above reaction rate can be expressed as

$$\dot{w} = \Lambda\rho Y_F \rho Y_O \exp\left(-\frac{\kappa(1-\theta)}{1-\vartheta(1-\theta)}\right) \tag{13}$$

with the following definitions

$$\theta = (T - T_0)/(T_\infty - T_0) , \quad \vartheta = (T_\infty - T_0)/T_\infty , \quad \kappa = \vartheta T_a/T_\infty , \text{ and } \Lambda = A\exp(-\kappa/\vartheta). \tag{14}$$

In the above expressions, T_0 is the inlet temperature and T_∞ is the adiabatic flame temperature of the stoichiometric mixture. The molecular weights of fuel and oxidizer are assumed to be equal and the chemical reaction rates of fuel and oxidizer are equal, i.e., $\omega_F = \omega_O = -\omega$.

The compressible Navier-Stokes equations along with the conservation equations for species and energy are solved in a two-dimensional domain. Spatial derivatives are approximated by a sixth-order compact finite-difference algorithm and the equations are integrated in time using a third-order Runge-Kutta scheme. Boundary conditions are specified using the Navier-Stokes Characteristic Boundary Conditions (NSCBC) [41]. The flame is stabilized using a procedure similar to the one implemented by Ruetsch et al [11]. A correction is applied to the streamwise component, u_1, of the velocity field that corresponds to the difference between the local displacement speed of iso-scalar surfaces near the reaction zone and along the centerline and its corresponding fluid velocity. The inlet velocity is adjusted accordingly. The mass fraction distributions of fuel and oxidizer are specified by using an error function profile as

$$Y_F = 1 - Y_O = \frac{1}{2}\left[1 - erf\left(\frac{y}{W}\right)\right], \tag{15}$$

where W is the characteristic mixing layer width, and y is assigned to be zero at the middle of the computational domain such that the plane with $y=0$ corresponds to the stoichiometric mixture. An outflow boundary condition is specified at the outlet of the computational domain and non-reflecting boundary conditions are imposed on all sides. The buoyancy is described by the Froude number based on the planar premixed flame speed and a characteristic length scale. This length is associated with distance over which dilatation occurs. For the computational conditions considered, this distance is related to the flame thickness because of the relatively moderate mixture fraction gradients used. However, if the mixture fraction gradient is increased, the scalar mixing layer width may also become an important parameter.

We will explore the relevance of two different Froude numbers associated with the scalar mixing layer width at the inlet, W, and the flame thickness, L_f. Based on W, we have

$$Fr_w \equiv \frac{S_L^2}{gW}.$$ (16)

Similarly, we replace W by the thickness of a planar stoichiometric premixed flame, L_f, we have another Froude number, Fr_{Lf}, as

$$Fr_{Lf} \equiv \frac{S_L^2}{gL_f}$$ (17)

Positive values of the Froude number (thereby of g) correspond to triple flames propagating into the direction where gravity force is pointed (downward propagating flame) and vice versa. Table 1 lists the conditions and the range of parameters computed in this study.

The numerical simulations for steady state triple flames were carried out with a uniform grid system of 121x241 grids (streamwise direction x transverse direction) with a physical region of about 40x80 flame thickness. Exploration runs with twice the resolution have been conducted showing differences within 1% in terms of deduced flame propagation speed. The steady-state solution of the triple flame structure is obtained using a similar numerical technique described by Ruetsch et al [11]. Steady state solutions without gravity force were obtained first and they were used as initial conditions for subsequent runs with buoyancy effects to save time.

Structure and Propagation of Stable Triple Flames

General Observations on Stable Triple Flames

The general characteristics of a triple flame are briefly described here to provide the necessary background for the discussions of the effects of buoyancy on triple flames. Figure 1 presents the computed contours of axial velocity and fuel consumption rate in a two-dimensional domain. The mixture enters the domain from the left side of the boundary. As seen in the reaction rate contour, the triple flame structure is delineated by its three branches. The two `wings' correspond to the two lean and rich premixed flames. The `tail' trailing the premixed branches corresponds to the diffusion flame branch where excess fuel and oxidizer from the premixed branches are burned. As the triple flame propagates upstream, the flow ahead of the triple flame tip is decelerated as streamlines diverge. As the flow approaches the reaction zone, heat release causes the flow to accelerate. Further downstream of the triple flame tip, the flow gradually decelerates as the flow behind the flame tip continues to expand laterally. In Figure 2, detailed contours of triple flame structures are shown in terms of temperature, reaction rate and species mass fraction.

Effects of Buoyancy on the Steady Triple Flame Structure

The above results serve as a baseline for comparison with triple flames subject to buoyancy effects. The computed global effects of buoyancy on triple flames are illustrated in Fig. 3 with $1/Fr_W=1$ (downward-propagating flame, top row), 0 (zero gravity baseline case, middle row), and -1 (upward-propagating flame, bottom row). Shown on the left side of the figure are iso-contours of mixture fraction (dashed lines), Z, defined as

$$Z = \frac{1+Y_F-Y_O}{2} \tag{18}$$

and streamlines (solid lines). The stoichiometric value for Z is 0.5 for the prescribed mixture properties. The corresponding reaction rate iso-contours superposed on temperature iso-contours are shown on the right hand side.

When the Froude number is positive, buoyancy enhances the flow acceleration above the triple flame tip as density decreases. The opposite effect occurs when the gravity force is reversed in direction. In comparison with the triple flame without gravity force, buoyancy results in a narrower triple flame when the gravity force is pointed downward. As the gravity force is reversed a wider span triple flame is seen. Therefore, the flame shape is affected by buoyancy and by the direction of the gravity vector. Moreover, due to buoyancy, the changes of the downstream flow field lead to modifications in the mixing layer ahead of the triple flame via flow field divergence such that its propagation speed is altered.

Detailed profiles of the mixture fraction gradient, temperature, and reaction rate along the stoichiometric line are shown in Fig. 4. Consistent with the qualitative flow pattern seen in Fig. 3 the mixture fraction gradient increases when the buoyancy accelerates the fluid above the triple flame tip. The opposite is seen when the Froude number is negative. The computed peak reaction rate and temperature at the triple flame tip are much less influenced by buoyancy. However, the reaction rate along the diffusion branch is seen to increase when the triple flame becomes narrower (cases with positive Froude numbers). This is due to increased diffusion of fuel and oxidizer as the triple flame gets narrow.

Steady Propagation of Triple Flames

In this investigation, the triple flame propagation properties are characterized by a single quantity, the triple flame propagation speed. This quantity measures the flame speed at the leading edge of the triple flame relative to the uniform upstream flow. Other definitions may be adopted as well. However, the triple flame speed is perhaps the most relevant quantity for triple flame stabilization.

The mechanism of triple flame speed enhancement under gravity

The propagation speed of the triple flame is computed by tracking an interface corresponding to a fixed fuel mass fraction along the centerline. The corresponding displacement speed of this interface along the centerline in the x direction relative to the local flow may be expressed by

$$S_D = \frac{\partial / \partial x (\rho D_F \partial Y_F / \partial x) + \dot{\omega}_F}{\rho |\partial Y_F / \partial x|}.$$ (19)

This speed measures the component of the fuel interface displacement in the x direction, and is valid only along the centerline. At steady state, S_D corresponds to the displacement speeds of other scalar iso-contours in the same location. To evaluate the triple flame propagation speed, the total speed of the iso-scalar contour at the triple flame tip (gas velocity plus displacement speed in the x direction), is subtracted from the cold flow velocity far upstream of the triple flame as

$$S_P = -[(u_1 - S_D) - u_0] = (S_D - u_1) + u_0$$ (20)

Here, u_1 is the flow velocity in the streamwise direction where S_D is evaluated, and u_0 is the unburned gas velocity in the streamwise direction evaluated at the inlet. As noted earlier, the value of u_0 is continually adjusted to stabilize the leading edge of the flame in one location. Therefore, the branches of the triple flame are allowed to evolve through their propagation properties and the flow field until the flame structure reaches its steady state. When the flow field reaches steady state, the inlet velocity, u_0, corresponds exactly to the triple flame speed. However, steady state of the triple flame structure is reached much earlier; and the above relation is valid much earlier than the simple relation of $S_p = u_0$. Maintaining the correction, $S_D - u_1$, in the above equation also reveals the fundamental mechanism of the enhancement of the triple flame propagation speed. Since u_1 is positive in the present study, a reduction in u_1 leads to an increase in the triple flame speed. The magnitude of u_1 is influenced by both flow divergence and buoyancy effects. Previous analytical and numerical studies of triple flame propagation (e.g., [6,11]) showed that the propagation speed decreases with increasing mixture fraction gradient due to the effects of flame curvature, but increases with heat release due to the divergence effects of the flow field.

Detailed profiles of the various contributions to the triple flame speed along the centerline are shown in Fig. 5 for $Fr_W = -1$, 0 and 1. As expected, buoyancy has a large effect on the flow field downstream of the triple flame tip, as it enhances flow acceleration in downward-propagating flames and reduces it for upward-propagating flames. However, the displacement speed is found to be less sensitive to buoyancy. As the definition of S_D indicates, the value of the displacement speed is governed by the balance of reaction and diffusion and the laminar flame thickness. Therefore, it is closely associated with molecular transport and chemistry in the reaction zone, quantities that are only marginally affected by buoyancy as suggested by results presented in the previous section. Therefore, changes in the value of S_p may be attributed primarily to hydrodynamic effects associated with flow acceleration by dilatation. Profiles of the triple flame propagation speed show that S_p is uniform over a relatively wide region around the peak of displacement speed. This is also the region where heat release occurs, providing a unambiguous location where the pertinent triple flame propagation quantities are evaluated. Consequently, we simply take the maximum

propagation speed evaluated along the stoichiometric line as the representative propagating speed. The propagation speed is reduced when the Froude number is positive.

Relation between Propagation Speed and Buoyancy

A series of simulations have been conducted to explore the relation between the triple flame propagation speed and the two different Froude numbers defined in Eqs. (16) and (17). A simplified analysis of the buoyancy effect on S_p is described in Appendix A and the result suggests the following relation in the limit of small gravity force

$$\frac{S_p}{S_{p,g=0}} \approx \left(1 - C_0 \frac{\rho_\infty}{\rho_0} \frac{1}{Fr_{Lf}}\right)^{1/2} \equiv \sqrt{1-X} , \tag{21}$$

where C_0 is a constant to be determined and $X \equiv C_0 (\rho_\infty / \rho_0)(1/Fr_{Lf})$. Although this correlation is limited to small values of the parameter, X, its predictions of the general trends of the triple flame propagation speed may extend beyond its underlying assumptions. First, the relation predicts the behavior of the flame at the limiting conditions of zero gravity by yielding a value on the left-hand side of unity. The expression also shows that the triple flame speed is enhanced by gravity in upward-propagating flames (gravity and propagation vectors are pointed in opposite directions) and reduced in downward-propagating flames (gravity and propagation vectors are aligned). Changes to the flame propagation speed is largely due to changes in the gas velocity in the expansion region as suggested already in Fig. 5. As in the original analysis of Ruetsch [11], lateral flow expansion is the primary mechanism for triple flame speed enhancement, and through which heat release (expressed here in terms of the density ration, ρ_∞ / ρ_0) appears in the expression for the triple flame speed. Buoyancy, then, acts to modulate this expansion by fluid acceleration or deceleration through the flame.

Finally, Eq. (21) suggests the existence of a critical Froude number for downward propagating flames for which the triple flame propagation speed approaches zero:

$$Fr_{Lf,critical} = C_0 \frac{\rho_\infty}{\rho_0} , \text{ or } g_{critical} = \frac{1}{C_0} \frac{\rho_0}{\rho_\infty} \frac{S_L^2}{L_f} . \tag{22}$$

The validity of the analysis may not hold at this limiting condition. However, such a critical value if it exists, may have consequences to a variety of applications where triple flames play a role. For example, the stabilization of lifted jet diffusion flames may be significantly hampered under vanishing propagation speeds near this critical value of the Froude number. Conditions where the triple flame speed approaches zero or even becomes negative have been predicted by the analysis of Dold et al [4] and later by Daou and Linan [15] under strong straining conditions. Additional observations of negative triple flame speeds (not shown here) have also been noted by the authors associated with the Kelvin-Helmholtz instabilities.

9

Results of the analysis are compared to the simulations summarized in Table 1. As the density ratio appears in Eq. (21), case D listed in Table 1 is conducted with ρ_∞ / ρ_0 being half of that in other cases in order to test the density ratio dependence. In addition, Cases E and F are conducted with different laminar flame speeds so that different sets of Fr_{Lf} can be used for assessing the validity of Eq. (21). Figure 6 presents a comparison of computed triple flame propagation speeds and the simplified model with $C_0=10$. The agreement is good except for large values of X where the assumption of small gravity force is not valid. Also indicated in the figure are the estimated ranges for stoichiometric methane-air combustion and those with a fuel mixture of 77% N_2 and 23% H_2 by volume. The latter has the same laminar flame speed as methane-air premixed flame but with a thickness about four times larger. These estimates are seen to fall into the regions where Eq. (21) is accurate. Consequently, Eq. (21) may be used as a semi-empirical correlation for estimating the effect of buoyancy on triple flames with practical fuels at gravity conditions ranging from 0 to earth gravity.

Effect of Gravity Orientation

Several runs were performed to explore the effects of the orientation of gravity with respective to the axial flow direction. Figure 7 shows a comparison of reaction rate contours for different gravity vectors. The magnitude of gravity is fixed but its orientation is varied every 45°. The shapes of triple flames are seen to distort from the symmetric profiles when the gravity vector is inline with the x-direction.

Effect of Differential Diffusion

The effect of differential diffusion between fuel and oxidizer is studied by assigning fuel Lewis number different from 1 while keeping the oxidizer Lewis number to 1. Figure 8 presents contour plots of reaction rates from results using different fuel Lewis numbers. In comparison with the case of neutral diffusion, the diffusion branch shifts either to the fuel (left side) or to the oxidizer side (right side) when the fuel Lewis number is smaller than or larger than 1. This behavior can be understood as fuel diffuses faster than oxidizer when $Le_F<1$ and the stoichiometric reaction zone will then shift to the fuel side. Also revealed in the comparison is the burning intensity at the flame tip. When $Le_F<1$, the flame burns more rigorously leading to higher flame propagation speed. The opposite is true when $Le_F>1$. In Figure 9, the computed propagation speed is plotted versus Le_F showing an increase trend with decreasing fuel Lewis number. Also compared in the plot are the corresponding results under constant density condition that gives a much stronger Lewis number dependence. The effect of density change caused by combustion increases the distance among the three branches and therefore reducing the gradient of mixture fraction. Differential diffusion effect becomes less when the gradient is reduced.

Triple Flame Stability

General Observations on Unstable Triple Flames

The numerical simulations for unsteady state triple flames were carried out with a uniform grid system of 361x481 grids (streamwise direction x transverse direction) with a physical region of about 120x160 flame thickness. Due the large domain, the computation time is 6 times of that for steady state flames. Table 2 lists the limited conditions explored in this investigation. Figure 10 shows snapshots of reaction rate contours superposed on vorticity contours for unstable triple flames at equal time intervals for Case I. The figure shows two extended vortices of opposite signs that straddle the diffusion branch of the triple flame and originate just downstream of the premixed branches. The time sequence shows that the shape of the diffusion branches, as well as the angle made by the premixed branches with the axial direction, changes and follows closely the vortex pair. The same temporal sequences show a clear coupling between the baroclinic vorticity generated just downstream of the premixed branches and the dynamics of the triple flame. Similar observations are made by Agarwal et al [22], suggesting that the vorticity field and its effects on the mean velocity field are closely associated with triple flame instabilities.

Figure 11 presents a time series of temperature evolution at several centerline locations downstream of the triple flame tip for Case I. The onset of unsteady modes is clearly seen and the similarity of the temporal development of temperature is noted at different locations. The computed magnitude of oscillation is seen to increase with downstream distance indicative of an unstable mode being amplified as it travels downstream. A fast Fourier analysis has been performed on the centerline temperature time series at each downstream location. The resulting power density spectrum (not shown) contains high level of noise due to the small samples of data. There are no identifiable features from the power density plots. Figure 12 presents various features of a unstable triple flame during the unsteady development. In the top left figure, the difference between the axial components of triple flame propagation speed and the fluid speed at the triple flame tip is plotted versus time. For steady-state stable triple flames, the difference would be zero as denoted by the horizontal line. As time progresses, the difference is negative most of time and it occasionally is positive. The magnitude increases with time leading to a unstable triple flame. In the simulation, the triple flame moves toward downstream and it eventually goes out of the computational domain. The angel between the triple flame propagation direction and the axial axis is shown in the upper right figure. The unstable mode is seen initially close to a sinusoidal profile and it later becomes distorted as nonlinear effects become important. The magnitude also increases with time but is limited to about 90 degrees. The relationship between the difference and the angel is examined in the lower left plot. The axial component of triple flame propagation speed is $U_{P1} = |U_p| \cos(a)$, where a denotes the angel. When triple flame's propagation direction deviates from the axial direction, the axial component becomes small due to the tilting of flame leading to a large difference. The magnitudes of triple flame propagation speed and the fluid speed at the local triple flame tip are plotted versus time in the lower right figure. It is clear that the local fluid speed is greater than the triple flame propagation speed most of time. Consequently, a stable flame cannot be sustained. We have investigated the possible development of a stable triple flame from a unstable mode. This simulation is performed by restarting a unstable run with the buoyancy

removed suddenly. Figure 13 presents the same results as in Figure 12 showing the reverse trends. A stable triple flame is recovered eventually from an initially unstable condition.

Linear Stability Analysis

In many respects, the analysis of triple flame stability may be implemented in the same fashion as previous analyses [21, 31]. Kimura [36] constructed a stability theory for axisymmetric parallel flows and showed that the oscillation of laminar-jet flames can be explained by linear stability analysis. Trouve and Candel [29] performed a linear stability analysis of the inlet jet in a ramjet dump combustor using hyperbolic-tangent velocity and temperature profiles. They found that the density variation has a significant effect in the instability. Jackson and Grosch [30] studied the effect of heat release in the spatial stability of a supersonic reacting mixing layer using the hyperbolic-tangent velocity profile and the flame sheet approximation. Mahalingam et al [31], studied the effects of heat release on the stability of coflowing, chemically reacting jets. They suggested that the heat release due to chemical reaction stabilizes the flow. Buckmaster and Peters [35] performed an inviscid linear instability analysis for a candle flame. The results are comparable with experimental results.

An inviscid linear stability analysis is implemented on the steady-state triple flame solutions obtained using the formulation of the previous sections. Although the buoyancy term has been included in the above formulation, it is neglected in the linear stability formulation below. Both viscous and buoyancy terms have been shown to be of the same order [35], and thereby the buoyancy term is neglected in the inviscid stability formulation. We also assume that the flow is parallel with its predominant flow direction in the x-axis. The parallel flow assumption implies that the predominant variation of the mean flow properties is in the spanwise direction. The flow variables, ρ, u, v, p, and temperature, T, are assumed to be the sum of the mean and a disturbance of the form

$$f(x,y,t) = \bar{f}(y) + f'(x,y,t),$$ (23)

where $f(x,y,t)$ is a generic flow variable that is a function of position and time. The over-bars and primes denote the mean and disturbance components, respectively. Because the parallel flow assumption is invoked, $\bar{f}$ is assumed to be a function of y alone.

The disturbance terms are described as traveling waves

$$f'(x,y,t) = \tilde{f}(y)\exp[i(\alpha x - \beta t)],$$ (24)

where the quantity $\tilde{f}$ is the eigenfunction assumed to be a function of y only; α is the complex streamwise wave number; β is the given temporal frequency; and i is defined by $i \equiv \sqrt{-1}$. For the temporal stability analysis, α is real and β is complex, whereas for the spatial stability analysis, α is complex and β is real. The amplification rates for the two cases are β_i and $-\alpha_i$, respectively. A detailed formulation of the stability analysis is provided in Appendix B. The analysis yields a second order ordinary differential equation for a transformation, Φ, of the pressure eigenfunction,

$\tilde{p}$ (see Appendix B). The pressure eigenfunction equation is solved using the shooting method for real β values and complex α values (the spatial stability analysis). Mean profiles of the temperature, density and velocity from numerical simulations of stable flames are fitted and used for the mean terms in the disturbances equations.

Figure 14 shows a typical result from the linear instability analysis based on steady state triple flames. The frequency, β, normalized by the width of mixing at the incoming flow and laminar flame speed, as a function of the negative imaginary part of the wave number, $-\alpha_i$ at a distance $3\frac{1}{3}$ mixing widths, W, downstream of the inlet and at two different Froude numbers (based on mixing width) and zero gravity. The figure show that as gravity effect increases (with Froude decreasing), the frequency at the most amplified mode increases in magnitude and shifts to higher wave numbers. Therefore, increasing gravity effect leads to less stable flames; this is consistent with numerical simulations of triple flames. The location of most amplified frequency at $3\frac{1}{3}W$ is found around 0.073 for $Fr_W = 2$, which is within less than 15% of the observed value in the numerical simulations of 0.083. For a given condition, the magnitude of the most amplified frequency is found to decreases with downstream distance. Therefore, the observed value from numerical simulations is more representative of conditions just downstream of the premixed branches. This further enforces the observation that instabilities are initiated just downstream of the premixed branches.

The effect of mixing width on the stability is examined in Figure 15 in terms of the frequency at the most-amplified mode from the linear stability analysis. The frequency is seen to increase with buoyancy effect but decrease with the mixing width. This appears consistent with the expectation that a thicker flame (with a larger mixing width) has a slower motion if the flame becomes unstable. Case N and Case O were performed to reveal the dependence of stability on the mixing width. When the mixing width is increased by 50% in Case O in comparison with Case I, the flame becomes stable consistent with the findings from the linear stability analysis. In Case O, we increase the effect of gravity by a factor of two while keeping other parameters as same as those in Case N, the triple flame becomes unstable. We have explored the effect of differential diffusion effects on the stability with limited runs for $Le_F = 0.4$ and $Le_F = 2.0$ (Case J and Case K) under the same gravity effect as the case of $Le_F = 1.0$ (Case I). Under the neutral diffusion, the triple flame becomes unstable. The flame with the smaller fuel Lewis number is stable while that with the higher Lewis number is unstable. A further run for $Le_F = 2$ with half of the gravity effect was also performed (Case L) and the results lead to a unstable triple flame. These limited runs suggest that the stability of triple flames is sensitive to the differential diffusion effects. As revealed in Fig. 9, the triple flame propagation increases with decreasing fuel Lewis number and this seems to correlate with the stability of the flame.

Conclusions

The influence of buoyancy on the propagation and structure of triple flames in a two-dimensional scalar mixing layer is studied numerically with a wide range of parameters, including the mixing width, the amount of heat release, and the magnitude of gravity force. The numerical

results revealed that buoyancy affects the triple flame topology, its propagation speed, and to a lesser extent its structure. When the gravity force is pointed in the direction of the triple flame (downward-propagating), buoyancy causes further acceleration of fluids downstream of the triple flame tip. In comparison to triple flames without buoyancy effects, the two premixed flame branches are brought closer to the diffusion branch leading to a less divergent flow pattern ahead of the triple flame. In response to the changes in fluid flow, the triple flame propagation speed decreases and the fuel consumption rate of the diffusion branch increases. The opposite trend is found for upward-propagating triple flames, where gravity force is pointed in the direction opposite to that of propagation. A simplified analytical model for the buoyancy effect on triple flame propagation speed is proposed for the limiting case of small gravity force. The analytical model is found in reasonably good agreement with the numerical results over a wide range of conditions including gravity, heat release, and mixing width. The analysis also suggests that for downward-propagating flames with a relatively large Froude number, the triple flame propagation speed approaches zero. This trend, which seems to occur beyond the limitation of the simplified model, shows encouraging comparisons with the numerical results. The existence of a zero-speed triple flame under buoyancy conditions may have important consequences on the stabilization mechanisms of diffusion flames. For constant density flows, differential diffusion effects are found to significantly affect the propagation speed. This finding is consistent with previous studies; however, heat release causes these effects to decrease due to fluid expansion.

The simulations show that downward-propagating (positive Froude numbers) flames exhibit instabilities at relatively strong gravity conditions. An inviscid linear stability analysis is implemented on the steady profiles of the velocity, temperature and density profiles. The analysis shows that the most amplified frequency increases with the value of the gravity force but decreases with the mixing width. The predicted most amplified frequencies from stability analysis is within a reasonable range of the instabilities frequencies observed in the two-dimensional simulations of the triple flames. The magnitude of this frequency is lower with downstream distance of the premixed branches further suggesting that the origin of these instabilities may be associated with the baroclinic vorticity generated by the premixed branches. Numerical exploration runs indicated that the stability of triple flames is sensitive to the fuel Lewis number. Triple flames with low fuel Lewis number are found more stable under the same conditions at which the triple flame is unstable with $Le_F=1$.

Acknowledgments

References

[1] Phillips H, *10th Int. Symp. on Combustion* (Pittsburgh, PA: Combustion Institute) pp.1227-1283, 1965.

[2] Dold, J.W., *Prog. Astro. and Aero.* 113:240-248 (1988).

[3] Dold, J.W., *Combust. Flame* 76:~71-88, (1989).

[4] Dold, J.W., Hartley, L.J. and Green, D., *IMA Volumes in Mathematics and its Applications* 35, Springer-Verlag 83-105, 1991.

[5] Buckmaster, J. and Matalon, M. *22nd Int. Symp. on Combustion* (Pittsburgh, PA: Combustion Institute) pp. 1527-1535, 1988.

[6] Hartley, L. J. and Dold, J. W., *Combust. Sci. and Tech.* 80: 23-46 (1991).

[7] Chung, S.H. and Lee, B.J., *Combust. Flame* 86: 62-72 (1991).

[8] Kioni, P.N., Rogg, B., Bray, K.N.C., and Linan., *Combust. Flame* 95:276-290 (1993).

[9] Lee B J, Kim, J S, and Chung S H, *25th Int. Symp. on Combustion* (Pittsburgh, PA Combustion Institute) pp. 1175-1181, 1994.

[10] Lee, B.J. and Chung, S.H. *Combust. Flame* 109:163-172 (1997).

[11] Ruetsch, G. R., Vervisch, L. and Linan, *Phys. Fluids* 7(6): 1447-1454 (1995).

[12] Ruetsch, G.R. and Ferziger, J.H. *Annual Research Briefs* Center for Turbulence Research NASA Ames, Stanford University, pp. 67--84, 1996.

[13] Domingo, P. and Vervisch, L. *26th Int. Symp. on Combustion* (Pittsburgh, PA: Combustion Institute) pp.233, 1996.

[14] Plessing, T., Terhoeven, P., Peters, N., and Mansour, M.S. *Combust. Flame* 115:335-353 (1998).

[15] Daou, J. and Linan, *Combust. Theo. Model.* 2:449-477 (1998).

[16] Echekki, T. and Chen, J.H., *Combust. Flame* 114:231-245 (1998).

[17] Ghosal, S. and Vervisch, L. *J. Fluid Mechanics* 415:227-260 (2000).

[18] Chen, Y.C. and Bilger, R.W. Stabilization mechanisms of lifted flames in axisymmetric jet flows, accepted by *Combust. Flame*, 2001.

[19] Im, H.G. and Chen, J.H. *Combust. Flame* 119:436-454 (1999).

[20] Poinsot, T. and Lele, S. *Computational Physics*, 101:104-129 (1992)

[21] Shin, D.S. and Ferziger, J.H., *AIAA Journal* 29(10):1634-1642 (1991).

[22] Aggarwal, S.K., Puri, I.K., and Qin, X. *Physics Fluids* 13(1):265-275 (2001).

[23] Rayleigh, Lord, *Proc. London Math. Soc.* 11:57-70 (1880).

[24] Lin, C.C., *The Theory of Hydrodynamic Stability*, Cambridge Univ. Press, Cambridge, England, UK, 1995.

[25] Michalke, A., *J. Fluid Mech.* 19:543-556 (1964).

[26] Monkewitz, P.A., and Huerre, P., *Physics of fluids* 25:1137-1143 (1982).

[27] Morkovin, M.V., " *Guide to Experiments on Instability and Laminar-Turbulent Transition in Shear Layers*," NASA Ames short course, 1998.

[28] Koochesfahani, M.M., and Frieler, C.E., *AIAA Paper* 87-0047, Jan. 1987.

[29] Trouve, A., and Candel, S.M., *AIAA Paper* 88-0149, Jan,1988.

[30] Jackson, T.L., and Grosch, C.E., *NASA* CR-181753, Nov. 1988.

[31] Mahalingam, S., Cantwell, B., and Ferziger, J., *AIAA Paper* 89-0691, Jan. 1989.

[32] Groppengiesser, H., *NASA* TF-12, 786, Feb. 1970.

[33] Blumen, W., Drazin,P. G., and Billings, D.F., *J. Fluid Mech.* 71:305-316.

[34] Sandham, N., and Reynolds, W., *AIAA Paper* 89--0371. Jan. 1989.

[35] Buckmaster, J. and Peters, N. *21st Symp. (Int.) on Combustion* (Pittsburgh, PA: Combustion Institute) pp.1829-1836, 1888.

[36] Kimura, I., *10th Symp. (Int.) on Combustion*, The Combustion Inst., Pittsburgh. PA, pp. 1295-1300, 1965.

[37] Anderson, K. R., Hertzberg, J. and Mahalingam, S., *Combust. Sci. Tech* 112:257-269 (1996).

[38] Chen, J.Y. and Echekki, T. *Proceedings of the Fifth Int. Microgravity Combustion Workshop*, NASA/CP report 1999-208917 pp. 427-430, 1999.

[39] Drazin, P.G., and Reid, W.H., *Hydrodynamic Stability*, Cambridge Univ. Press, Cambridge, England, UK, pp. 129-132, 1982.

[40] Long M B, Walsh K T, and Smooke M D , *Proc. of the Fifth Int. Microgravity Combustion Workshop*, NASA/CP report 1999-208917 pp. 105-110, 1999.

[41] Poinsot T and Lele S, *J. Comput. Phys.* 101:104-129 (1992).

[42] McMurtry, P.A., Jou, W.H., Riley, J.J., and Metcalfe, R.W., *AIAA Paper* 85-014 (1985).

[43] Tzuoo, K.S., Ferziger, J.H., and Kline,S.J., *Mechanical Engineering, Report TF-27*, Stanford University, CA, Nov. 1986.

[44] Sandham, N.D., and Reynolds, W.C., *Mechanical Engineering, Report TF-45*, Stanford University, CA, Sept. 1989.

[45] Huerre, P., and Monkewitz, P.A., *J. of Fluid Mech.* 159:151-168 (1985).

[46] Mahalingam, S., Cantwell,B.J., and Ferziger, J.H., *Mechanical Engineering, Report TF-43*, Stanford University, CA, Aug. 1989.

Appendix A: Simplified Analysis of Buoyancy Effects on Triple Flames

In the following analysis, we derive an expression for the leading-order dependence of the triple flame speed on buoyancy. The analysis follows closely the derivation and assumptions adopted by Ruetsch et al [11]. The results are derived in the limit of small Froude numbers or small gravity force relative to flow inertia due to heat release. Figure 16 shows a schematic of a triple flame subject to a gravity force pointed downward with stations 1-4, denoting different locations along the central streamline corresponding to far upstream (1) and downstream (4) of the reaction zone and points across the reaction zone (stations 2 and 3). Here, we assumed that (1) the flow at stations 1 and 4 is uniform in the lateral direction, and that (2) the dominant mechanisms for velocity changes are governed by lateral flow divergence/convergence for the portions of streamline between 1 and 2 and between 3 and 4, and by flow dilatation or heat release across stations 2 and 3. We have used g to represent the magnitude of the gravity vector, and its value may be positive (downward-propagating flame) or negative (upward-propagating flame). Here, we are concerned primarily with the velocity component in the streamwise direction, u_1. The notation is further simplified by dropping the subscript, 1, associated with the streamwise direction. Instead the subscripts used in the analysis refer to the downstream locations along the centerline.

Using the Rankine-Hugoniot relation across the points 2 and 3, we have

$$\rho_2 u_2 = \rho_3 u_3 \qquad (25)$$

$$p_2 + \rho_2 u_2^2 = p_3 + \rho_3 u_3^2. \tag{26}$$

Here, p, u and ρ correspond to the static pressure, flow velocity along the stoichiometric streamline and the gas density, respectively. Note that for the stabilized (in laboratory coordinates) triple flame, the triple flame propagation speed, S_p is equal to u1. If the flame structure is not altered by the geometry of the triple flame, its consumption speed evaluated at the triple point is equal to the planar laminar flame speed, S_L, and the velocity at station 2, u_2. Also, consistently with the notation adopted in the text, the densities ρ_1 and ρ_4 correspond to the upstream and downstream densities, ρ_0 and ρ_∞, respectively. Along the streamline at the center, Bernoulli's equation gives the following results for segments from point 1 to point 2 and from point 3 to point 4

$$p_1 + \frac{1}{2} \rho_1 u_1^2 + \rho_1 g x_1 = p_2 + \frac{1}{2} \rho_2 u_2^2 + \rho_2 g x_2 \tag{27}$$

$$p_3 + \frac{1}{2} \rho_3 u_3^2 + \rho_3 g x_3 = p_4 + \frac{1}{2} \rho_4 u_4^2 + \rho_4 g x_4 \tag{28}$$

Let's denote $L_1 = x_2 - x_1$ and $L_2 = x_4 - x_3$, and assume that $\rho_1 = \rho_2$, $\rho_3 = \rho_4$, and $\rho_1 u_1 \delta_1 \approx \rho_4 u_4 \delta_4$. With these assumptions, we can combine Eqs. (25)-(28) leading to the following result

$$\left(\frac{u_1}{u_2}\right)^2 = \frac{\frac{\rho_1}{\rho_4} - 1}{\frac{p_1 - p_4 - (\rho_1 L_1 + \rho_4 L_2)g}{\frac{1}{2}\rho_1 u_1^2} - \frac{\rho_1}{\rho_4}\left(\frac{\delta_1}{\delta_4}\right)^2 + 1}. \tag{29}$$

The difference between the background hydrostatic pressures without combustion at point 4 and point 1 is $p_{s,1} - p_{s,4} = \rho_1(L_1 + L_2)g$. Expressing the pressure as $p = p_s + p'$, we can rewrite Eq. (29) as

$$\left(\frac{u_1}{u_2}\right)^2 = \frac{\frac{\rho_1}{\rho_4} - 1}{\frac{p'_1 - p'_4 + (\rho_1 - \rho_4)L_2 g}{\frac{1}{2}\rho_1 u_1^2} - \frac{\rho_1}{\rho_4}\left(\frac{\delta_1}{\delta_4}\right)^2 + 1} \tag{30}$$

Ruetsch, et al [11] assumed $p'_1 \approx p'_4$ and $u_1 \approx u_4$ for triple flames without buoyancy effects. In the limit of small gravity force, these assumptions are applicable and the following result emerges

$$\left(\frac{u_1}{u_2}\right)^2 = \frac{\frac{\rho_1}{\rho_4} - 1}{\frac{(\rho_1 - \rho_4)2L_2 g}{\rho_1 u_1^2} - \frac{\rho_4}{\rho_1} + 1} = \frac{\rho_1}{\rho_4} \frac{1}{\frac{2L_2 g}{u_2^2}\left(\frac{u_2^2}{u_1^2}\right) + 1}. \tag{31}$$

Solving for u_1/u_2, we obtain

$$\frac{u_1}{\sqrt{\frac{\rho_1}{\rho_4}} u_2} = \sqrt{1 - \frac{\rho_4}{\rho_1} \frac{2L_2 g}{u_2^2}}. \tag{32}$$

For triple flames without gravity force (g=0), Eq. (32) reduces to $u_1 = \sqrt{\rho_1/\rho_4}\, u_2$ or in terms of the triple flame speed,

$$\frac{S_{p,g=0}}{S_L} \approx \sqrt{\frac{\rho_0}{\rho_\infty}}. \tag{33}$$

This relation is identical to that from the analysis by Ruetsch, et al [11] that provides an estimate of the effect of flow divergence on propagation speed. A simple relation repressing the ratio of the triple flame speed to the corresponding value at zero gravity may also be obtained

$$\frac{S_p}{S_p(g=0)} = \sqrt{1 - \frac{\rho_\infty}{\rho_0} \frac{2L_2 g}{S_L^2}} \tag{34}$$

In this relation, the right-hand are input parameters with the exception of the length scale, L_2. This quantity may be interpreted as a characteristic distance over which dilatation occurs, which, in turn, may be related to the flame thickness, L_f. However, a number of valid definitions of the flame thickness may be adopted based on unburned conditions as well as the profiles of the temperature or the reaction progress variable. In the following analysis, we assume that L_f and L_2 are related through a constant, C_0 such that, $L_2 = C_0 \, L_f/2$. This constant may be evaluated from calibration of numerical and experimental results, and may be related to the mixture's thermo-diffusive properties. The second factor, 0.5, is used to absorb the additional factor, 2, in Eq. (34). By substitution of this relation into Eq. (34), we obtain the following expression of the triple flame speed enhancement due to buoyancy as a function of laminar flame parameters and the gravity constant

$$\frac{S_p}{S_p(g=0)} \approx \sqrt{1 - C \frac{\rho_\infty}{\rho_0} \frac{\delta_1}{W} \frac{L_f g}{S_L^2}} \approx \sqrt{1 - C_0 \frac{\rho_\infty}{\rho_0} \frac{1}{Fr_{L_f}}}. \tag{35}$$

Appendix B: Inviscid Linear Stability Formulation and Numerical Solution

By substitution of the split terms in to the governing equations (without buoyancy or viscous terms), and linearization, we obtain the following governing equations for the eigenfunctions:

18

$$i\tilde{\rho}(\alpha U - \beta) + \tilde{v}\rho' + \rho(\tilde{v}' + \tilde{u}i\alpha) = 0, \tag{36}$$

$$-i\beta\rho\tilde{u} + \rho\tilde{v}U' + \rho Ui\alpha\tilde{u} = -i\alpha\tilde{p}, \tag{37}$$

$$-i\beta\rho\tilde{v} + \rho Ui\alpha\tilde{v} = -\tilde{p}', \tag{38}$$

$$i(\alpha U - \beta)\rho\tilde{T} + \rho T'\tilde{v} = 0, \tag{39}$$

$$\rho\tilde{T} + T\tilde{\rho} = 0, \tag{40}$$

where the prime, ', now denotes a derivative, d/dy, in the spanwise direction, y. The quantities U, ρ, and T represent the non-dimensional mean streamwise velocity, density, and temperature, respectively. The quantities $\tilde{\rho}$, $\tilde{u}, \tilde{v}, \tilde{p}$, and $\tilde{T}$, denote the non-dimensional density, x and y velocity components, pressure, and temperature eigenfunctions, respectively. Note that all of the quantities, including y, are dimensionless. The quantities α and β are the complex streamwise wave number and the temporal frequency, respectively.

An eigenfunction for the pressure may be obtained by combining the continuity and momentum eigenfunction equations

$$\tilde{p}'' - \frac{2\alpha U'}{\alpha U - \beta}\tilde{p}' + \tilde{\rho}(\alpha U - b)^2 - \alpha^2\tilde{p} = 0. \tag{41}$$

Elimination of the density term in the above equation may be done using the energy and ideal gas state equations, to yield

$$\tilde{p}'' - \left(\frac{2\alpha U'}{\alpha U - \beta} - \frac{T'}{T}\right)\tilde{p}' - \alpha^2\tilde{p} = 0. \tag{42}$$

Boundary conditions for $\tilde{p}$ at $y=\pm\infty$ may be obtained by inspecting the governing equations at the limits of the governing equation $y=\pm\infty$

$$\tilde{p}'' - \alpha^2\tilde{p} = 0, \tag{43}$$

which admits a solution of the form

$$\tilde{p} = C_1 e^{\alpha y} + C_2 e^{-\alpha y} = C_1 e^{(\alpha_r + i\alpha_i)y} + C_2 e^{-(\alpha_r + i\alpha_i)y}. \tag{44}$$

C_1 and C_2 are arbitrary complex constants and without loss of generality, $\alpha_r \geq 0$. The pressure eigenfunction as y approaches $\pm\infty$ may be expressed as follows

$$y \rightarrow +\infty : \tilde{p} = C_2 e^{-(\alpha_r + i\alpha_i)y}, \tag{45}$$

$$y \rightarrow -\infty : \tilde{p} = C_1 e^{(\alpha_r + i\alpha_i)y}, \tag{46}$$

because the solution of the pressure eigenfunction is bounded when $y \rightarrow \pm\infty$. The second order pressure eigenfunction equation may be simplified to a first order equation for a related eigenfunction, Φ, obtained using a Ricatti transformation (e.g. Michalke [25]):

$$\tilde{p}(y) \equiv C e^{\int^y \Phi(\eta)d\eta}. \tag{47}$$

19

Again, C is an arbitrary complex constant. This transformation yields a complex constant, C, for the value of $\tilde{p}$ at y=0. Therefore, the solution for $\tilde{p}$ is determined within a constant. Thus, from the transformation, Eq. (47), we have

$$\tilde{p}'(y) \equiv Ce^{\int \Phi(\eta)d\eta}\Phi = \tilde{p}\Phi, \quad \tilde{p}''(y) = (\tilde{p}\Phi)' = (\Phi' + \Phi^2)\tilde{p}. \tag{48}$$

Substituting Eq. (48) into the pressure eigenfunction equation and deleting the common factor $\tilde{p}$, we obtain the Φ eigenfunction equation:

$$\Phi' + \Phi^2 - \left(\frac{2\alpha U'}{\alpha U - \beta} - \frac{T'}{T}\right)\Phi - \alpha^2 = 0 \tag{49}$$

Since both the Φ eigenfunction and streamwise wave number α are complex whereas the temporal frequency β is real for spatially developing flows, we can split Φ into the real and imaginary parts, respectively:

$$\Phi = \Phi_r + i\Phi_i, \ \alpha = \alpha_r + i\alpha_i. \tag{50}$$

To obtain the governing equations for Φ_r and Φ_i, we substitute Eq. (50) into Eq. (49) and split the eigenfunction equation into the real and imaginary parts as

Real part:

$$\Phi'_r + \Phi_r^2 - \Phi_i^2 + A\Phi_r - B\Phi_i - \alpha_r^2 + \alpha_i^2 = 0, \tag{51}$$

Imaginary part:

$$\Phi'_i + 2\Phi_r\Phi_i + A\Phi_i + B\Phi_r - 2\alpha_r\alpha_i = 0, \tag{52}$$

where

$$A(y) = \frac{T'}{T} - \frac{2U'[\alpha_r(\alpha_r U - \beta) + \alpha_i^2 U]}{(\alpha_r U - \beta)^2 + (\alpha_i U)^2}, \tag{53}$$

$$B(y) = \frac{2U'\alpha_i\beta}{(\alpha_r U - \beta)^2 + (\alpha_i U)^2}, \tag{54}$$

and $U(y)$ and $T(y)$ represent the dimensionless mean streamwise velocity and temperature, respectively.

The boundary conditions for the Φ_r and Φ_i eigenfunctions can be derived from the boundary conditions for the pressure eigenfunctions, Eqs. (51) and (52), and the transformation, Eq. (47). We have $\tilde{p}' = \tilde{p}\Phi$, that is,

$$\tilde{p}'/\tilde{p} = \Phi = \Phi_r + i\Phi_i \tag{55}$$

The boundary conditions at y=±∞ for Φ may be obtained using the simple expressions for $\tilde{p}$ at those limits, to yield:

$$y \to +\infty : \Phi_r = -\alpha_r, \ \Phi_i = -\alpha_i, \tag{56}$$

20

$$y \to -\infty : \Phi_r = \alpha_r, \quad \Phi_i = \alpha_i \tag{57}$$

Finally, the governing equations in the infinity physical domain, y, may be further simplified using a transformed finite domain coordinate system, $\xi : [-1,1]$, by using the transformation:

$$\xi = \tanh(s \cdot y), \tag{58}$$

where s is a stretching constant and

$$\tanh(x) = \frac{\sinh(x)}{\cosh(x)} = \frac{e^x - e^{-x}}{e^x + e^{-x}}. \tag{59}$$

Thus, we have

$$y = \frac{1}{2s} \ln \frac{1+\xi}{1-\xi}, \tag{59}$$

$$\frac{d\xi}{dy} = s \sec^2(sy) = s(1-\xi^2), \tag{60}$$

$$\phi'(y) = \frac{d\phi(y)}{dy} = \frac{d\phi(\xi)}{d\xi} x \frac{d\xi}{dy} = s(1-\xi^2)\dot{\phi}, \tag{61}$$

where $\dot{\phi}$ is defined by $d\phi/d\xi$ and ϕ is any generic quantity, for example, Φ_r, Φ_i, U, T, etc.

By substituting these transformations into the governing equations for Φ_r and , Φ_i (51) and (52), we obtain the corresponding governing equations in the transformed finite domain ξ: [-1,1]:

$$F(\xi) = s(1-\xi^2)\dot{\Phi}_r(\xi) + \Phi_r^2(\xi) - \Phi_i^2(\xi) + A(\xi)\Phi_r(\xi) - B(\xi)\Phi_i(\xi) - \alpha_r^2 + \alpha_i^2 = 0, \tag{62}$$

$$G(\xi) = s(1-\xi^2)\dot{\Phi}_i(\xi) + 2\Phi_r(\xi)\Phi_i(\xi) + A(\xi)\Phi_i(\xi) + B(\xi)\Phi_r(\xi) - 2\alpha_r\alpha_i = 0, \tag{63}$$

where

$$A(\xi) = \frac{s(1-\xi^2)\dot{T}(\xi)}{T(\xi)} - \frac{2s(1-\xi^2)\dot{U}(\xi)[\alpha_r(\alpha_r U(\xi) - \beta) + \alpha_i^2 U(\xi)]}{(\alpha_r U(\xi) - \beta)^2 + (\alpha_i U(\xi))^2}, \tag{64}$$

and

$$B(\xi) = \frac{2s(1-\xi^2)\dot{U}(\xi)\alpha_i\beta}{(\alpha_r U(\xi) - \beta)^2 + (\alpha_i U(\xi))^2} \tag{65}$$

From the boundary conditions for the $\Phi_r(y)$ and $\Phi_i(y)$ eigenfunctions, the corresponding boundary conditions for the $\Phi_r(\xi)$ and $\Phi_i(\xi)$ eigenfunctions on the computational domain ξ. [-1 , 1] are obtained:

$$\xi = 1 : \Phi_r = -\alpha_r, \quad \Phi_i = -\alpha_i, \tag{66}$$

$$\xi = -1 : \Phi_r = \alpha_r, \quad \Phi_i = \alpha_i, \tag{67}$$

where $\alpha_r \geq 0$.

Eigenfunction equations, Eqs. (51) and (52), with the corresponding boundary conditions, Eqs. (66) and (67), can be solved numerically by the shooting method for initial value problems [39]. Mean profiles of temperature, velocity and density are specified using fitted profiles of these quantities from the steady simulations. For the spatially developing flows, we specify the value of β (real) and an initial guessed value of α (complex) and integrate the above two equations from $\xi =$ -1 to 0 and from $\xi = 1$ to 0. The solutions are matched at $\xi = 0$ by adjusting the value of α leading to different boundary conditions for Φ at $\xi = 1$ and $\xi = -1$. The change of Φ is determined by the Newton iteration method. Convergent solutions of Φ_r and Φ_i eigenfunctions are obtained when the change of α becomes very small. The shooting method is reasonably fast and each run only takes a few minutes on a Pentium 500 MHz machine.

After obtaining the solutions of Φ_r and Φ_i eigenfunctions, we may recover the pressure eigenfunction by using the transformation (47):

$$\tilde{p}(y) \equiv C_3 e^{\int_{\xi}^{\eta} \Phi(\eta) d\eta} + C_4, \tag{68}$$

where C_3 and C_4 are constants. The integration was carried out in the computational domain from $\xi = 1$ to a certain point corresponding to y. Since the stability equation for the pressure eigenfunction is linear, any C_3 and C_4 may satisfy the governing equation. We set the values of C_3 and C_4 to 1 and 0, respectively.

Appendix C: Publications and Personnel

1. J.-Y. Chen and T. Echekki, "Numerical Study of Buoyancy and Differential Diffusion Effects on the Structure and Dynamics of Triple Flames" Proc. 5th Int. Microgravity Combustion Workshop, NASA/CP report 1999-208917 , pp. 427(1999).

2. J.-Y. Chen and T. Echekki, "Numerical Study of Buoyancy Effects on Triple Flames," Presented at the 2000 Western States Spring Meeting/The Combustion Institute, March 13-14, Paper number WS 00S-11, 2000.

3. J.-Y. Chen and T. Echekki, "Numerical Study of Buoyancy Effects on the Structure and Propagation of Triple Flames," Combustion Theory and Modelling, 5; 499-515 (2001).

4. J.-Y. Chen, T. Echekki, and U. Hegde, "Effect of Gravity on Triple Flame Propagation and Stability," 2nd Joint Meeting of the U.S. Sections of the Comustion Institute, Oakland, CA, March, paper # 177, 2001.

5. J.-Y. Chen, T. Echekki, and U. Hegde," Effects Of Gravity On Triple Flame Propagation and Stability" Proc. 6th Int. Microgravity Combustion Workshop, NASA/CP report 20001-210826 pp. 349 (2001).

6. Qianlong Liu, "Invisid Instability Analysis of Triple Flames," Thesis for Master of Engineering, December, 2001.

Personnel Supported by the Grant:

1. Professor J.-Y. Chen
2. Dr.Tarek Echekki (Postdoc researcher)
3. Mr. A. Permana (Doctoral candidate)
4. Mr. Qianlong Liu (Master of Engineering candidate to be awarded M.E. degree December, 2001)

Table 1 Simulation Conditions*

Case	ϑ	W/L_f	$S_L/S_L(A)$	ρ_0/ρ_∞	$1/Fr_{Lf}$
A	0.85	2	1	6.67	($-1.0\rightarrow0.5$)
B	0.85	4	1	6.67	($-0.5\rightarrow0.5$)
C	0.85	8	1	6.67	($-1.0\rightarrow0.625$)
D	0.70	4	1	3.34	($-1.0\rightarrow0.5$)
E	0.85	3.2	0.8	6.67	($-0.938\rightarrow0.547$)
F	0.85	4.8	1.2	6.67	($-0.417\rightarrow0.365$)

*Under all conditions, the Zel'dovich number is 8. ϑ is the heat release parameter that corresponds to the ratio between the flame temperature to the difference between the flame temperature (denoted with subscripts ∞) and unburnt gas temperature (denoted with subscripts 0) at stoichiometric conditions. W is the scalar mixing layer width. All flame speeds shown are normalized with the value in case A. ($a\rightarrow b$) corresponds to a range of values between a and b.

Table 2 Simulation Conditions for unsteady triple flames

Case	Fr_{Lf}	Fr_w	W/L_f	Le_F	Flame Mode
G	4	3	1.33	1	Stable
H	3	2.25	1.33	1	Unstable
I	2.67	2	1.33	1	Unstable
J	2.67	2	1.33	0.4	Stable
K	2.67	2	1.33	2.0	Unstable
L	5.32	4	1.33	2.0	Unstable
M	4	3	1.33	1.5	Unstable
N	4	2	2	1	Stable
O	2	1	2	1	Unstable

Normalized Streamwise Velocity
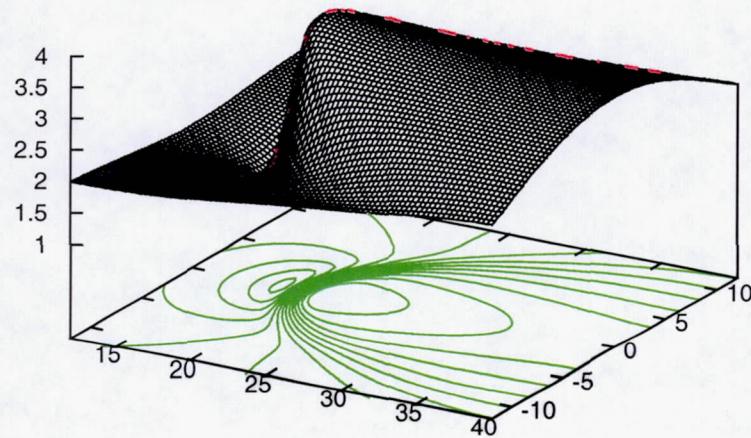
Normalized Fuel Consumption Rate
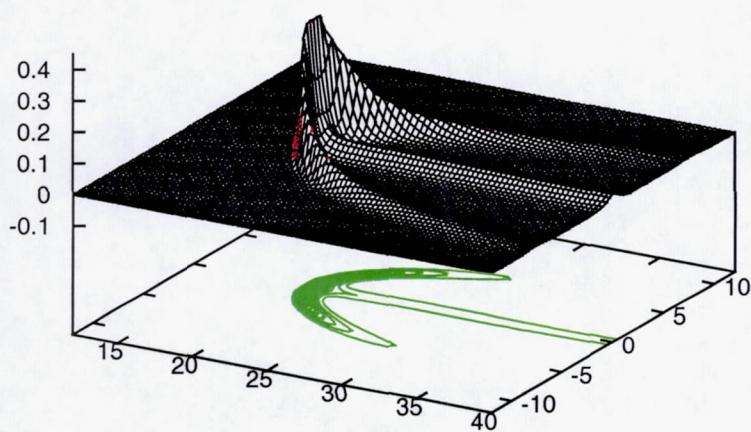
Fig. 1 Characteristics of triple flames obtained with a two dimensional simulation with inlet flow coming from the left and leaving to the right. A mixing layer of fuel and oxidizer is imposed on the inlet. Lengths are units of premixed flame thickness. Top: streamwise velocity normalized by premixed stoichiometric flame speed. Bottom: fuel consumption rate.
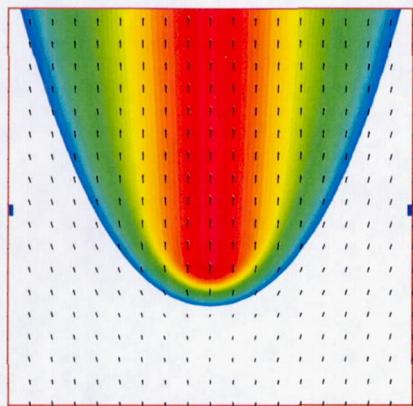
Temperature
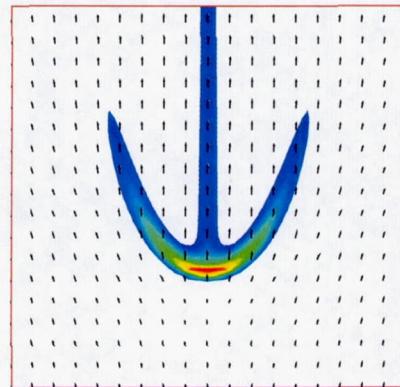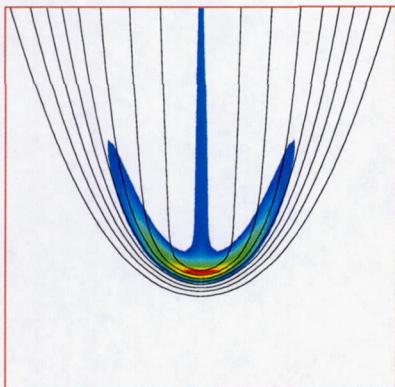
Reaction Rate
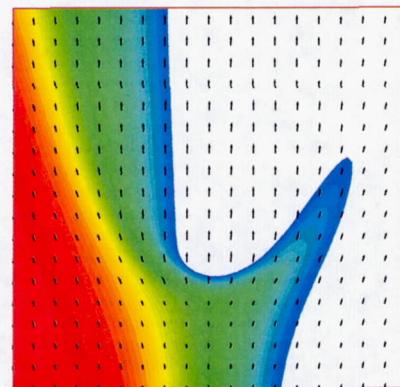
Temperature- Reaction Rate   Reactant Mass Fraction

Fig. 2 Contour plots of triple flame structures. The triple flame tip has highest burning rate clearly marked by the two premixed branches and the trailing diffusion branch. Flow divergence is seen by the arrows representing the velocity vectors.
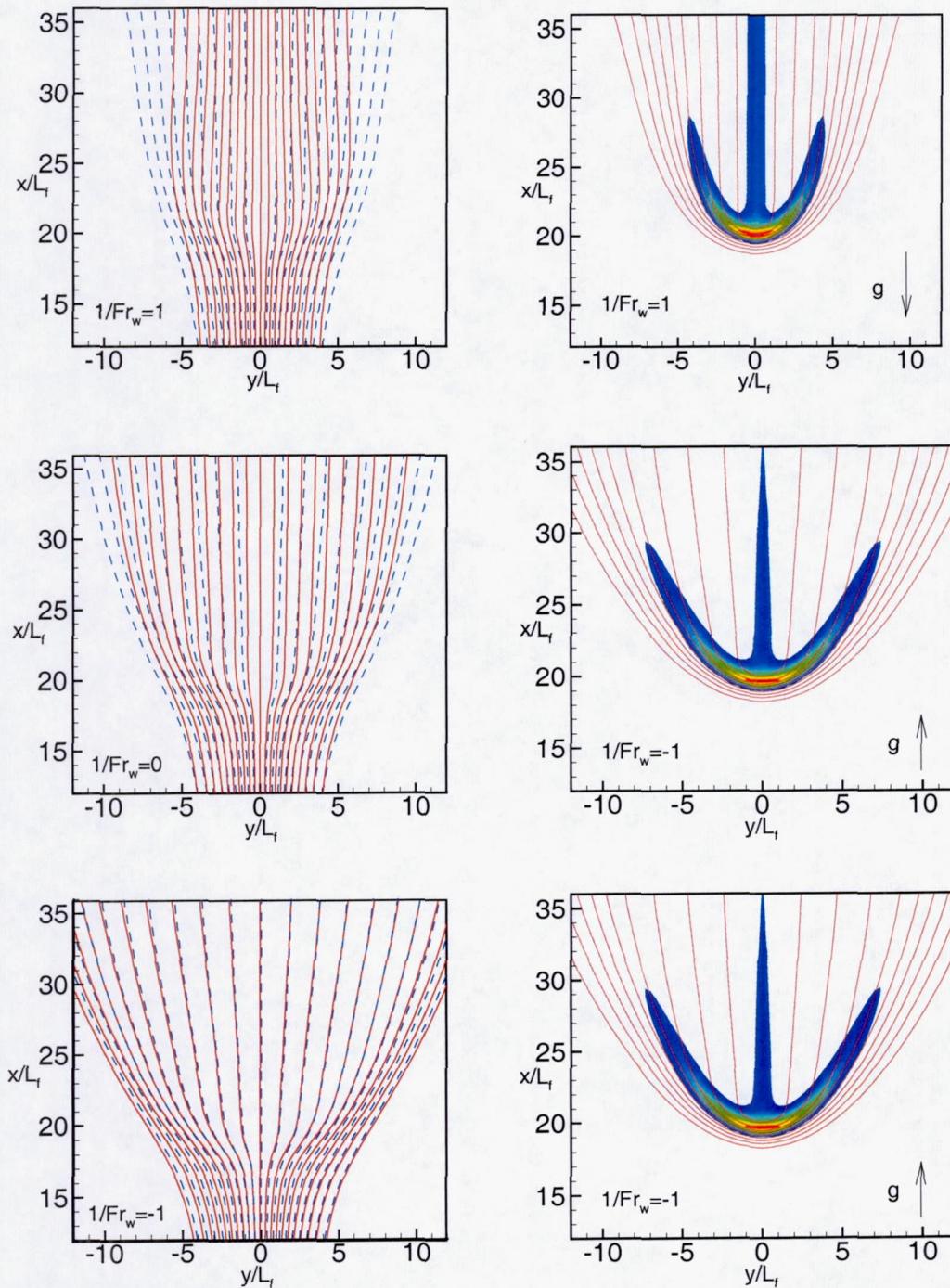
Fig. 3 Effects of buoyancy on triple flames in views of streamlines (solid) and constant mixture fraction contours (dashed lines) on left and reaction rate overlapped by constant temperature (lines) on right. Top: with gravity force pointed downward in the same direction of triple flame propagation (downward-propagating flame); middle: without a gravity force; bottom: with gravity force pointed upward in the opposite direction of triple flame propagation (upward-propagating flame). Lengths are units of premixed flame thickness.
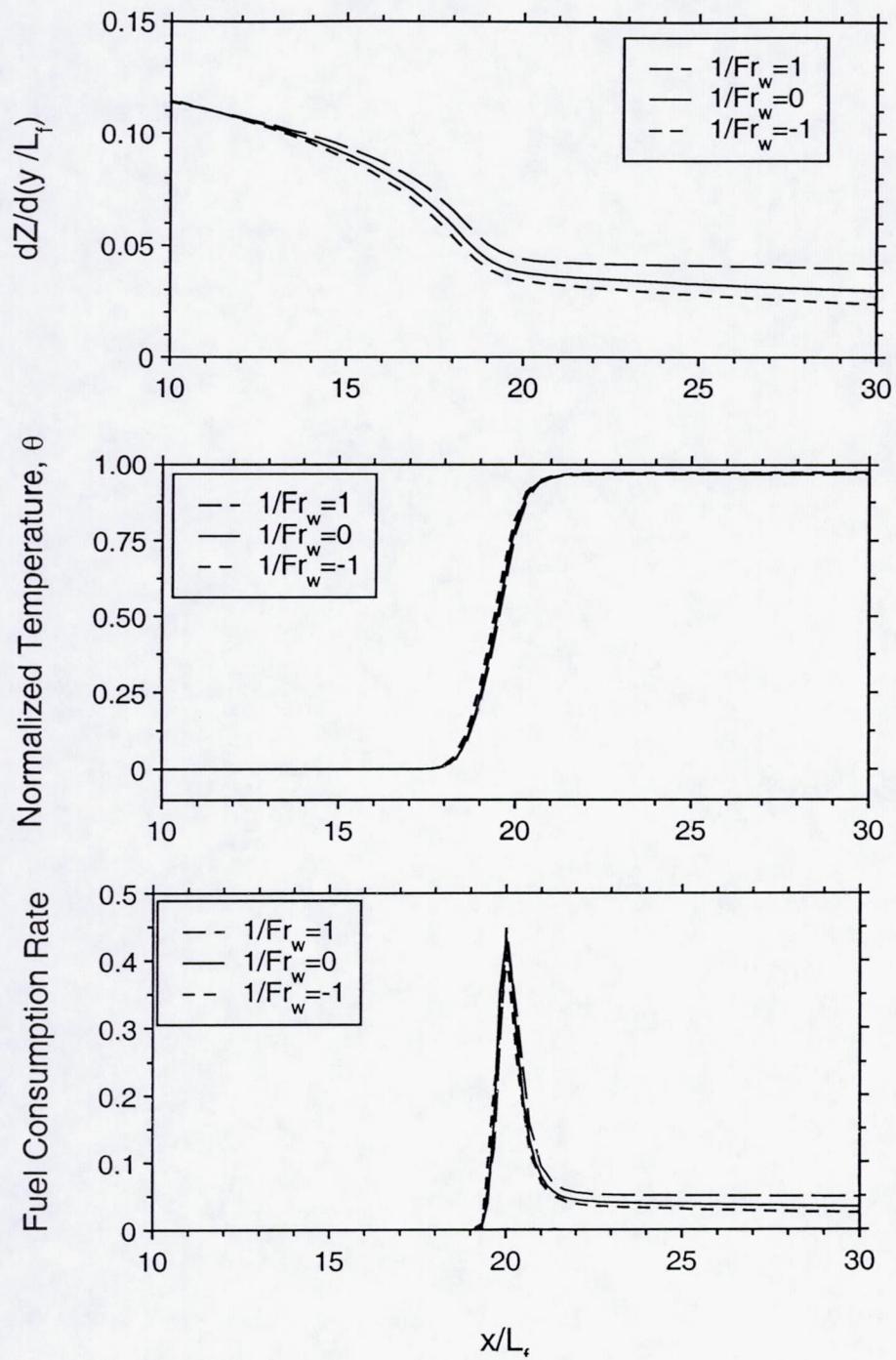
Fig. 4 Effects of buoyancy on triple flame structures along the stoichiometric line ($y=0$, $Z=0.5$). Simulations with gravity forces pointed downward ($Fr_W = 1$) and upward ($Fr_W = -1$). Reference case without gravity force ($Fr_W = 0$). Top: normalized mixture fraction gradient in the transverse flow direction; middle: normalized temperature; bottom: normalized fuel consumption rate.
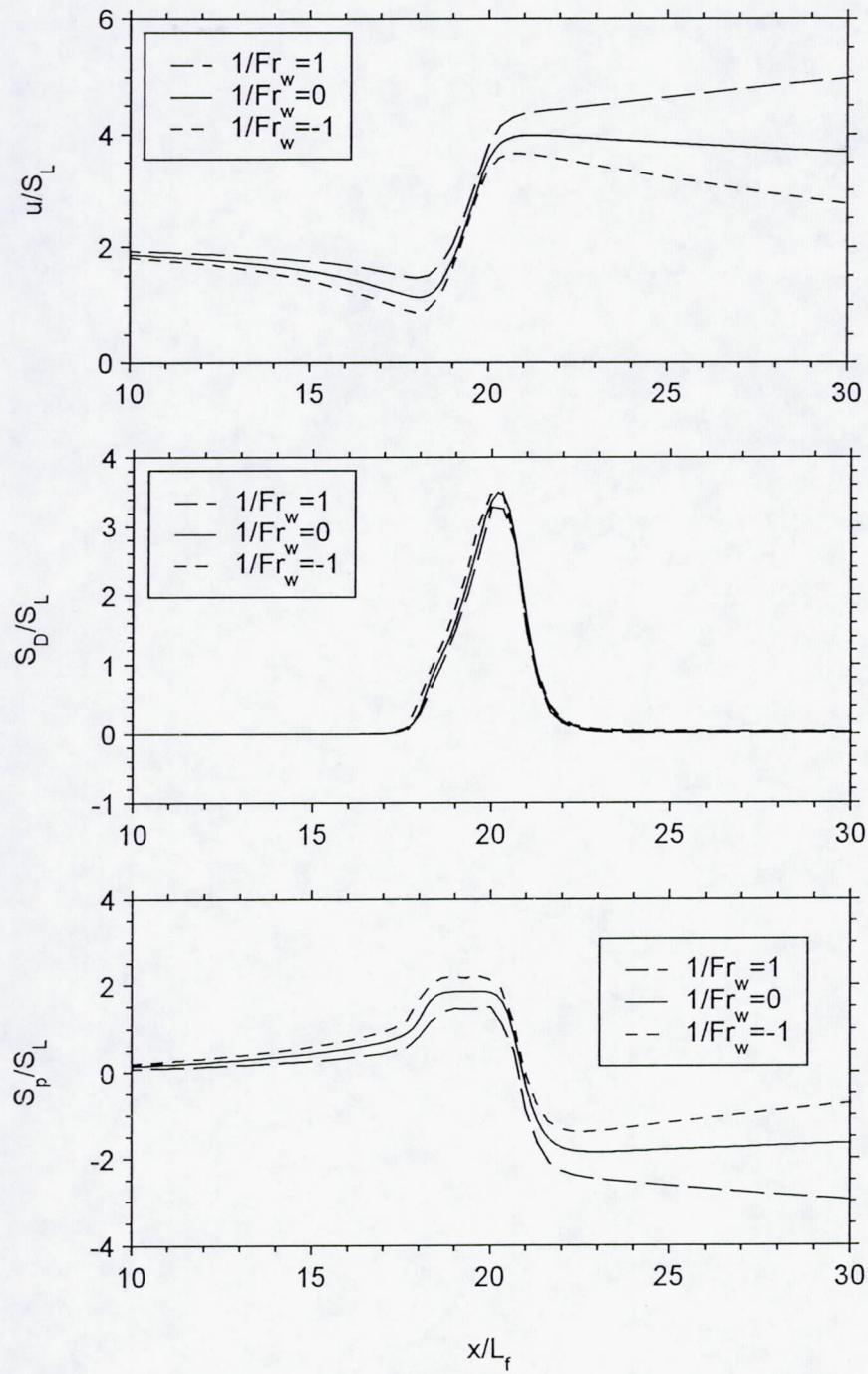
Fig. 5 Effects of buoyancy on characteristic velocities along the stoichiometric (centerline at y=0). Simulations were conducted without gravity force ($Fr_W = 0$) and with gravity forces pointed downward ($Fr_W = 1$) and upward ($Fr_W = -1$). Top: streamwise velocity; middle: displacement speed; bottom: triple flame propagation speed. All speeds are normalized by planar premixed stoichiometric flame speed.
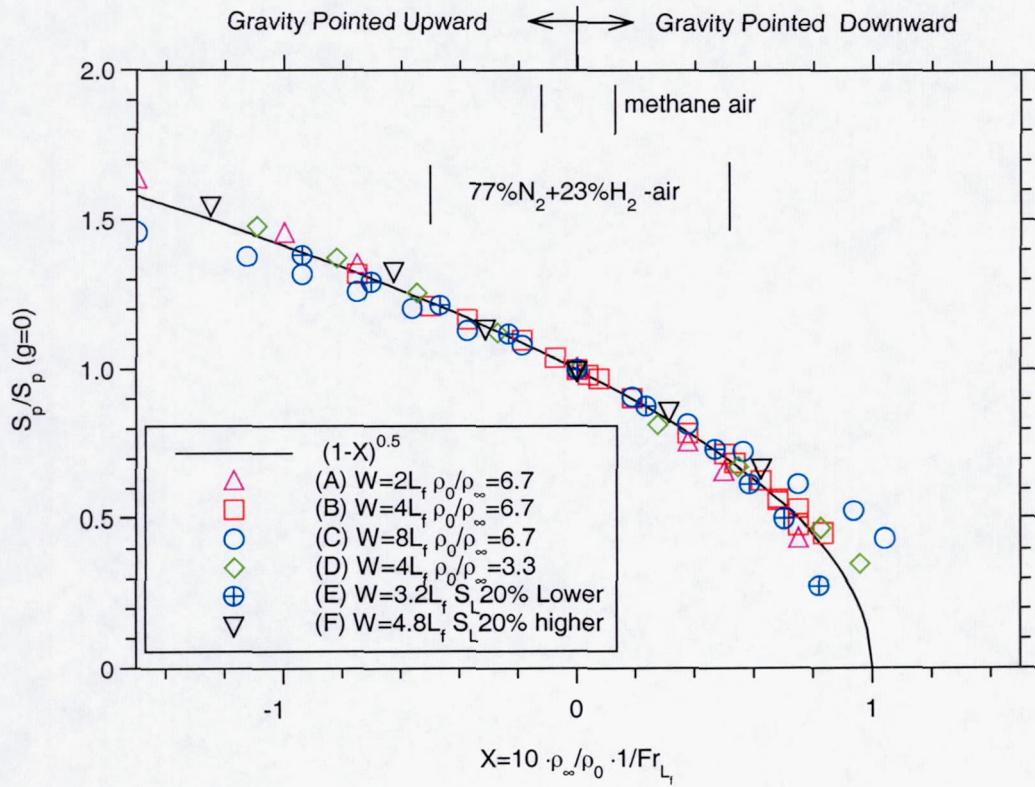
Fig. 6 Computed correlation between triple flame propagation speed normalized by its value at zero gravity and the Froude number based on the flame thickness of planar premixed stoichiometric flame. The triple flame propagates downward and the gravity forces are either pointed upward or downward. Details of conditions are listed in Table 1. The relations are seen to collapse onto one curve closely represented by Eq. (21).
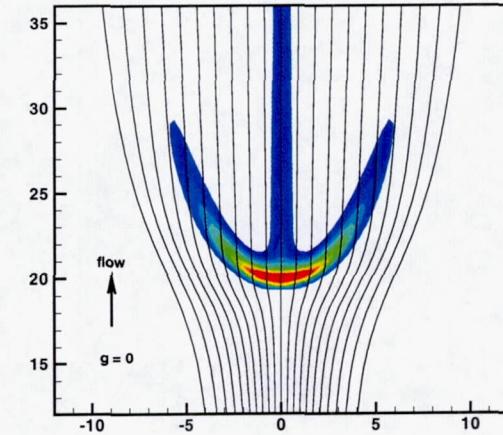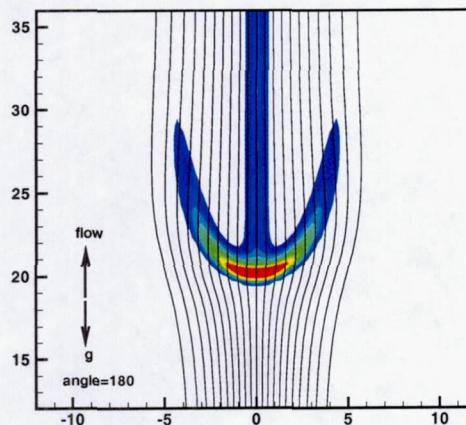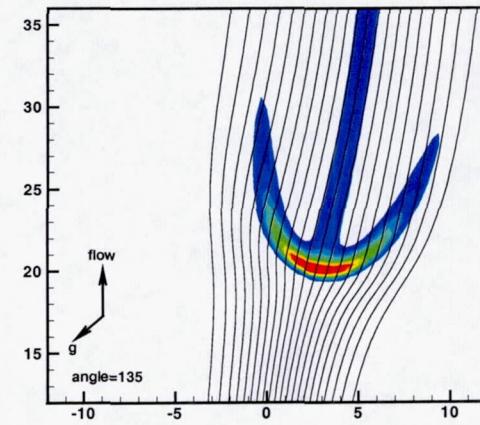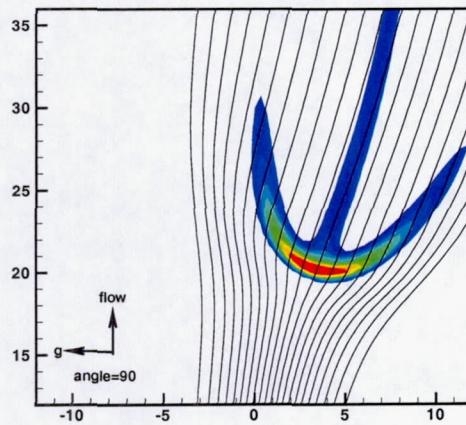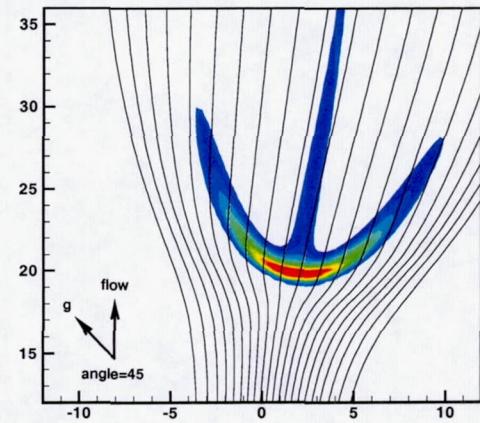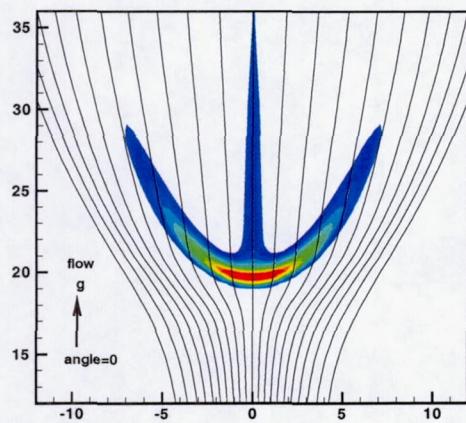
Fig 7 Effect of orientation of gravity on triple flames plotted as reaction rate contours overlapped by streamlines. The magnitude of gravity force is fixed while the orientation of gravity forces is varied every 45 degrees showing a strong impact of gravity on the shape.
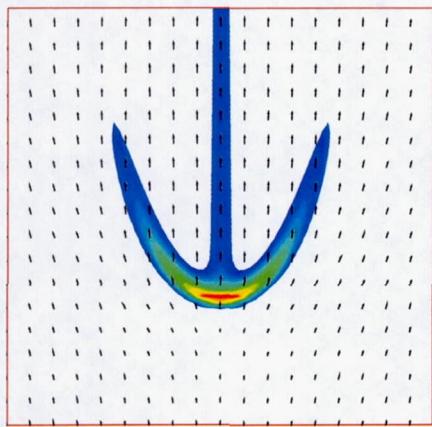
Le=1.0 Zero Gravity
$V_f/V_{sl}=1.92$
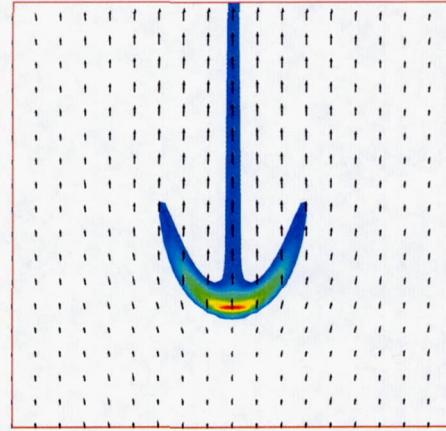
Le=1.0   Fr=1.0
$V_f/V_{sl}=1.26$
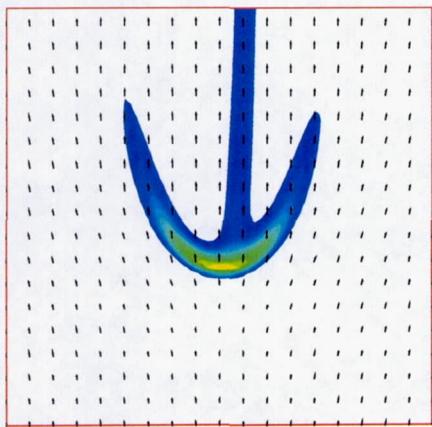
Le=2.0 Zero Gravity
$V_f/V_{sl}=1.20$
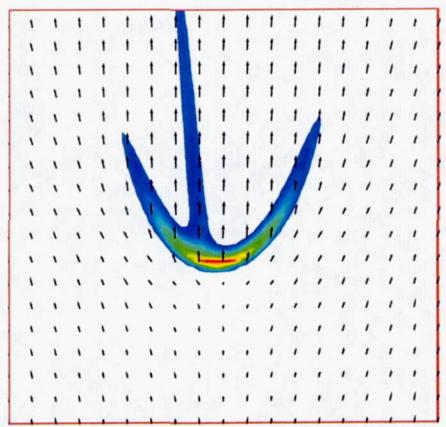
Le=0.4 Zero Gravity
$V_f/V_{sl}=3.07$

Fig. 8 Contour plots of reaction rates with various fuel Lewis number showing the effect of differential diffusion. An increase in triple propagation speed is seen as the fuel Lewis number decreases. V_f represents the flame propagation speed, and V_{sl} is the planar flame speed corresponding to a stoichiometric mixture.
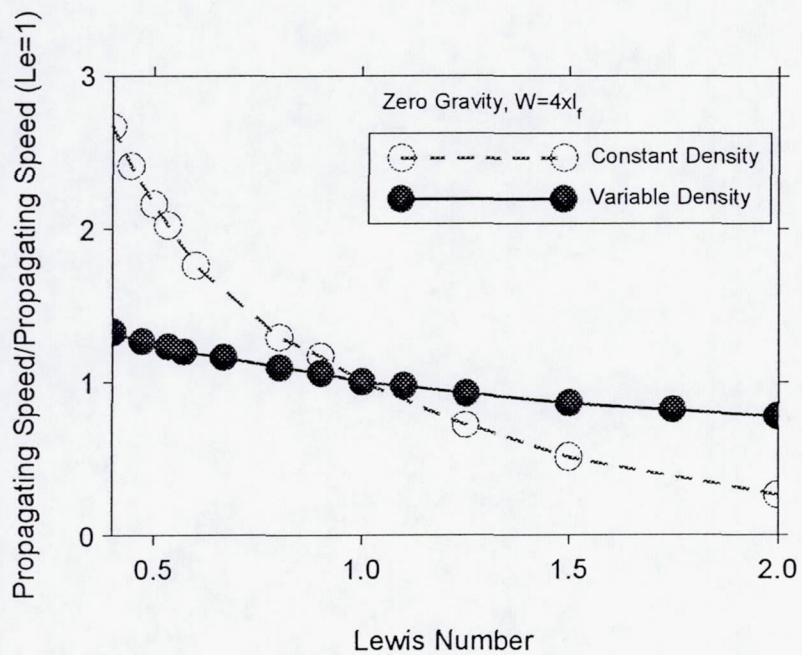
Fig. 9 Effect of differential diffusion in terms of fuel Lewis number showing that propagation speed increases with decreasing Lewis number. Heat release effect from combustion (density variation) decreases the effect of differential diffusion on the flame propagation speed.
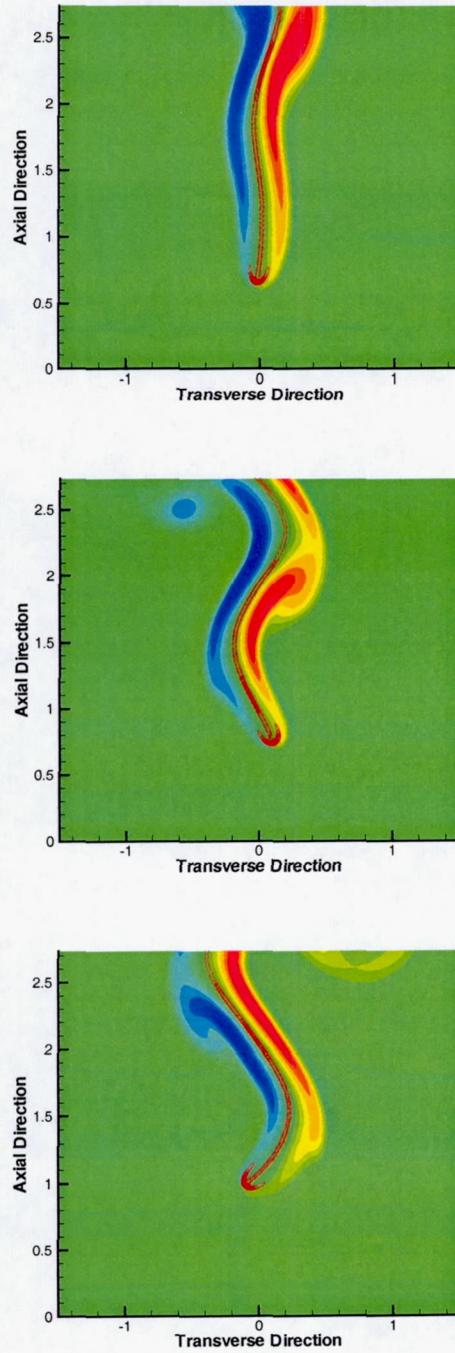
Fig. 10 Snapshots of reaction rate contours superposed on the vorticity field at different equally spaced times of the evolution of the unstable triple flame. The vorticity is indicated with blue for negative (counterclockwise) vorticity and red for positive vorticity.
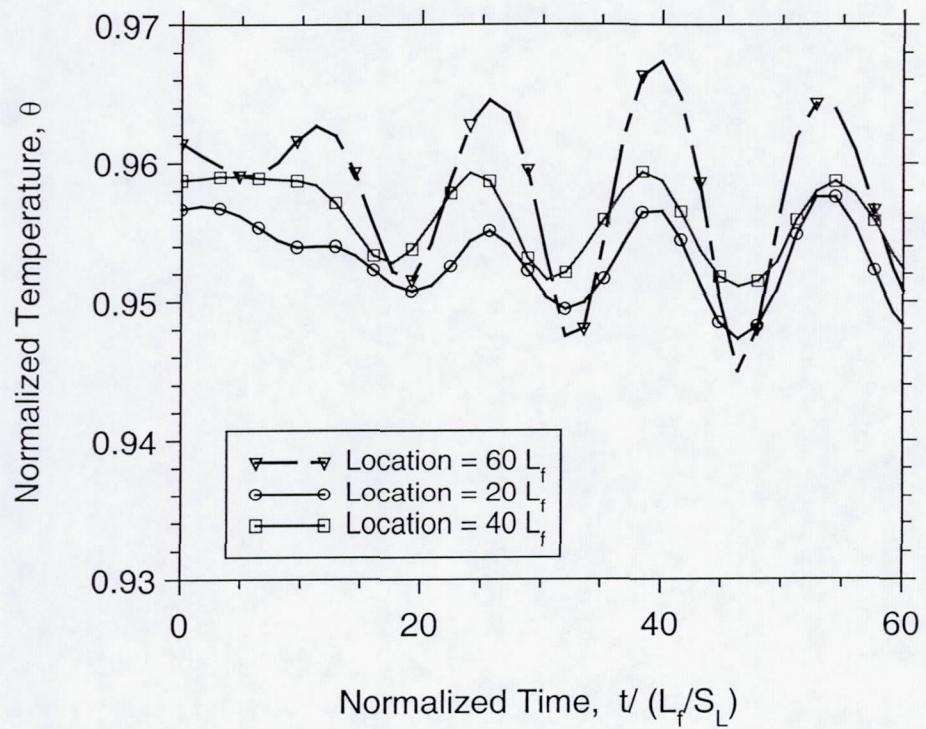
Fig. 11 Centerline temperature development of a triple flame undergoing unsteady evolution subject to buoyancy effect. Temperature profiles at different locations downstream of triple flame tip show similarity and the magnitude of oscillations are amplified downstream.
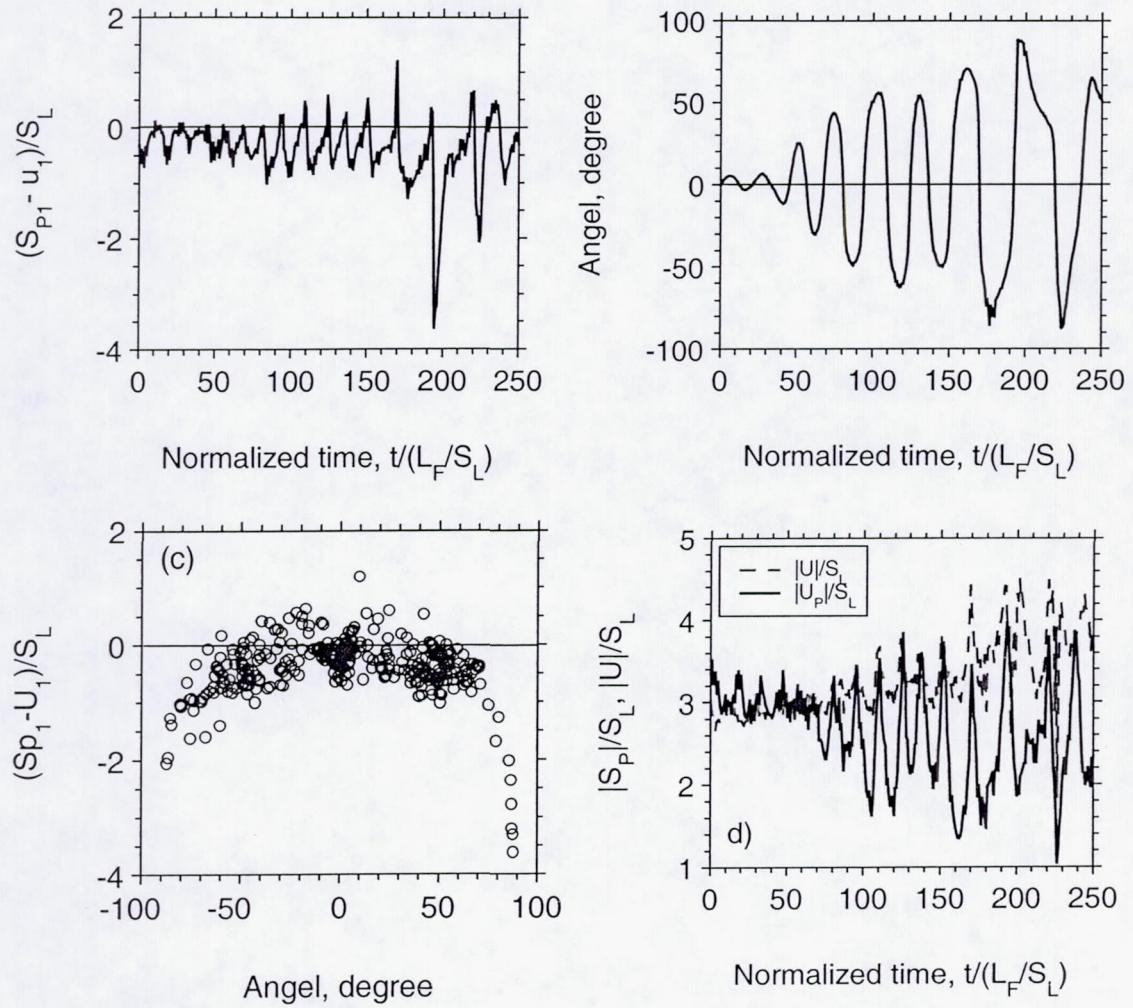
Fig. 12 Features of a unstable triple flame under unsteady development with a strong buoyancy effects. The axial component of triple flame propagation speed is found to be less than axial fluid velocity at the triple flame tip. A stable triple flame cannot be sustained due to the difference in the triple flame propagation speed and local fluid velocity.
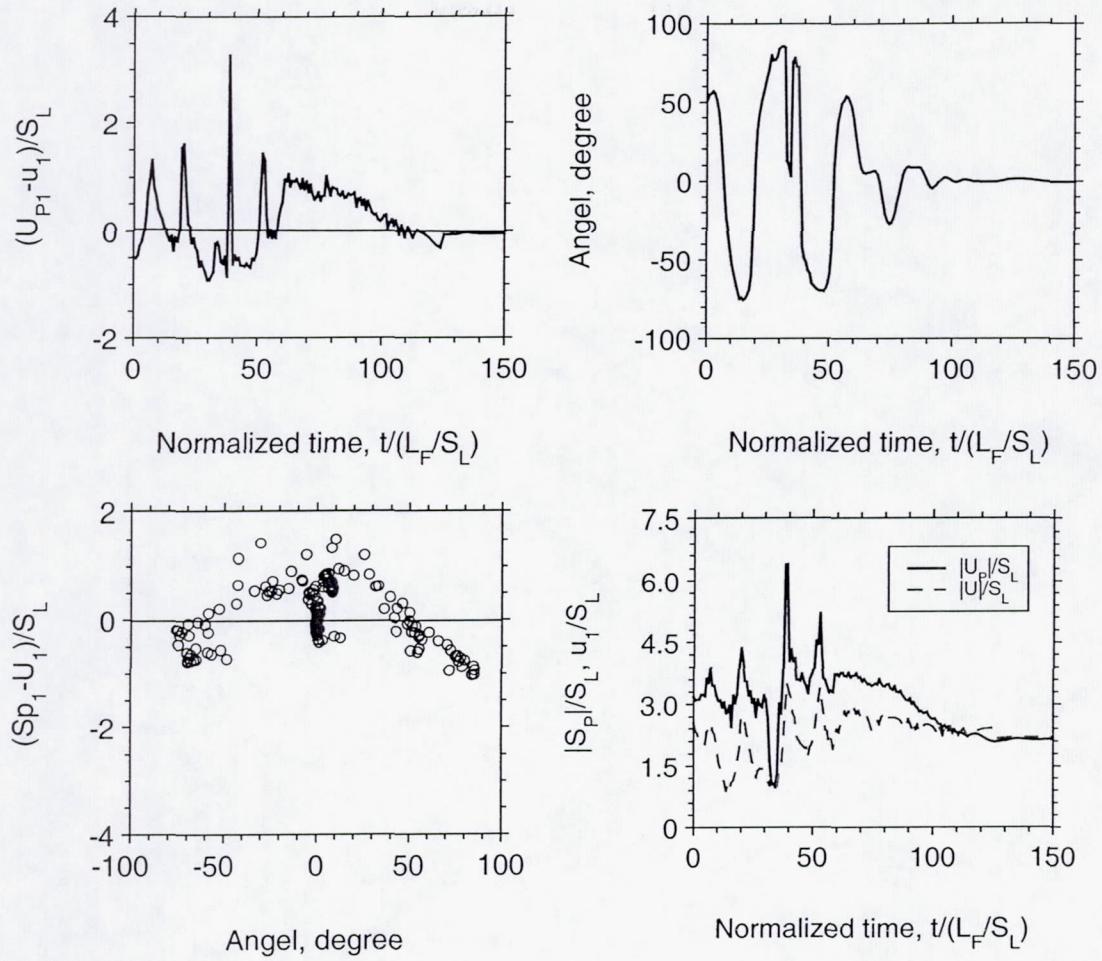
Fig. 13 Features of a unsteady triple flame under stable development by removing buoyancy effects. The axial component of triple flame propagation speed is found to be greater than axial fluid velocity at the triple flame tip. A stable triple flame is developed as the difference in the triple flame propagation speed and local fluid velocity becomes negligibly small.
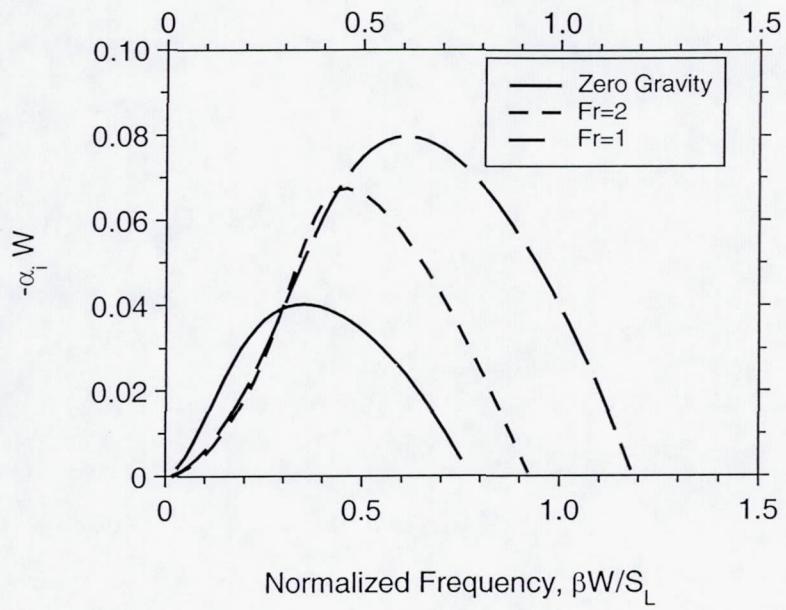
Fig. 14 Computed values of the negative wave number, $-\alpha_i$, for triple flames under various degree of gravity effect at a downstream location of $3\frac{1}{3}$ W. When gravity effect increases (reducing Froude number), the triple flame becomes less stable as the most amplified mode increases in magnitude.
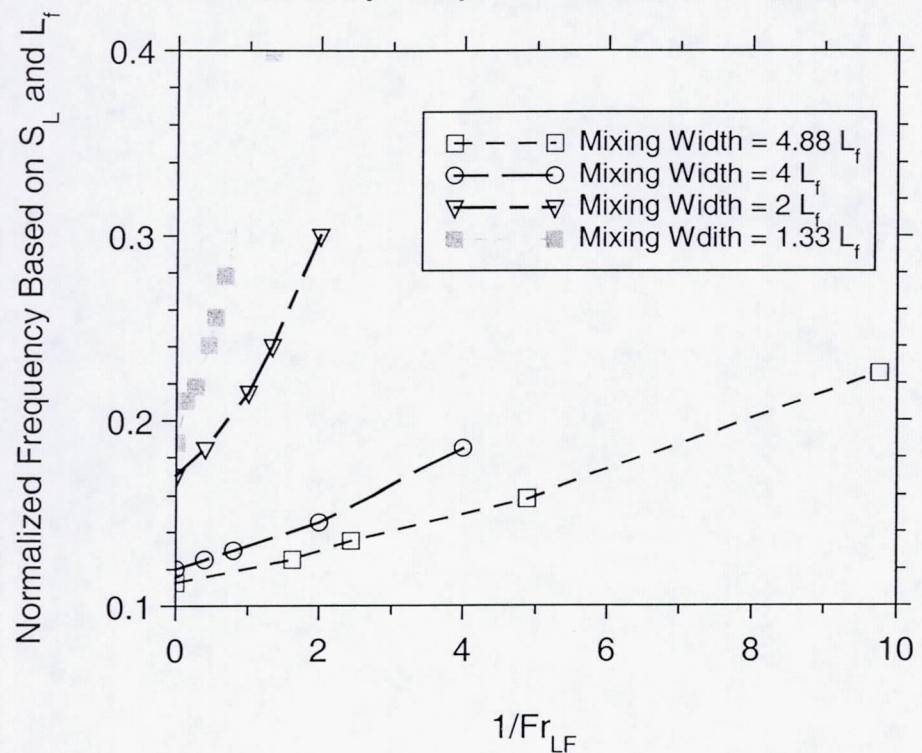
Fig. 15 Computed values of frequency at the most amplified mode for steady state triple flames under various degree of gravity effect at a downstream location of 2.5 *W*. The frequency increases with gravity effect (reducing Froude number) but decreases with the mixing width.
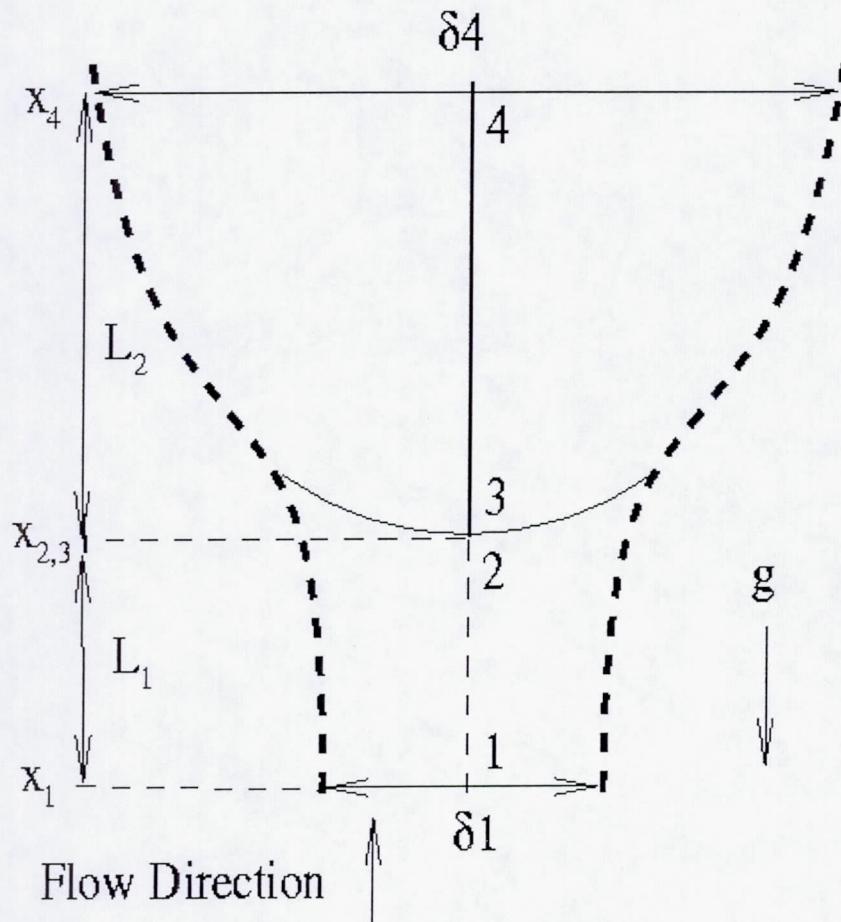
Fig. 16 Schematic of a triple flame subject to gravity force pointed downward in the same direction as the triple flame propagation. Heavy dashed lines: streamlines enclosing the triple flame; thick solid lines: triple flames anchored at point 2 with segment 3-4 denoting the trailing diffusion flame branch and the arc representing the two premixed flame branches. Distance L_2 is the size of region most affected by buoyancy force due to density changes. δ_1 and δ_4 are the sizes of stream tube at point 1 and 4 respectively.